Extension of the δ-Plus-SPH model for simulating Vortex-Induced-Vibration problems

P.N. Sun, A. Colagrossi, David Le Touzé, A.-M. Zhang

Version of Record: https://www.sciencedirect.com/science/article/pii/S0889974619301203
Manuscript_bc7aee69a0f4ff56857cdb8f021811f7

Extension of the δ-*Plus*-SPH model for simulating Vortex-Induced-Vibration problems

P.N. Sun[a], A. Colagrossi[b,a,*], D. Le Touzé[a], A.-M. Zhang[c]

[a] *Ecole Centrale Nantes, LHEEA res. dept. (ECN and CNRS), Nantes, France*
[b] *CNR-INM (INstitute of Marine engineering), Rome, Italy*
[c] *College of Shipbuilding Engineering, Harbin Engineering University, Harbin, China*

Abstract

In this paper, the Lagrangian particle method δ-*Plus*-SPH model is used to solve a series of benchmark test-cases of vortex induced vibrations (VIV). An Adaptive Particle Refinement (APR) technique is adopted to resolve correctly the boundary layer regions of the moving bodies, and to de-refine the particles that are transported far away. Furthermore, a switch correction on the pressure forces term is adopted in the momentum equation to completely remove the occurrence of the so-called *Tensile Instability* that leads to the development of numerical cavitation in negative pressure regions. Because of the Lagrangian nature of the method, difficulties arise when intense vortex wakes, typically developed in VIV problems, cross the outflow boundary. To this purpose, a damping zone is also implemented close to the outlet to improve the numerical stability of the scheme. The fluid-structure coupling technique is based on ghost particles properly generated inside the solid bodies. The validation is performed against test-cases for which reference solutions are available in the literature. Within those test-cases challenging benchmarks involving small mass ratios, large-amplitude body motions and multi-body interactions have been selected. For all the benchmark test-cases the δ-*Plus*-SPH results are in good agreement with the reference solutions, demonstrating the ability of this particle method in solving complex VIV problems.

Keywords: smoothed particle hydrodynamics, δ-*Plus*-SPH model, fluid-solid interaction, vortex induced vibration, tensile instability

*Corresponding author: *Tel.: +39 06 50 299 343; Fax: +39 06 50 70 619.*
Email address: andrea.colagrossi@cnr.it (A. Colagrossi)

1. Introduction

The vortex shedding due to the viscous flow separation is an important engineering topic because of the induced structure vibrations which can compromise the structure safety (Williamson and Govardhan, 2004). So far many experimental studies and numerical investigations have been carried out and different test-cases can be found in literature for the validation of the numerical codes , see Williamson and Govardhan (2008); Bearman (2011) and Wu et al. (2012).

Among the mesh-based numerical solvers, such as the Finite Volume Method (FVM) or the Finite Element Method (FEM), mesh distortions caused by large body displacements can limit the range of applicability only to problems with small translational and rotational motions, see Robertson et al. (2003). A further difficulty can arise for VIV problems involving multi-bodies, since the reciprocal movements of the bodies require a continuous adaptation of the meshes. To overcome such difficulties advanced coupling techniques, such as the Chimera (overset grid) one, are needed (Wang et al., 2017).

Conversely, when using boundary element method (BEM) or mesh reduction methods (MRM), the problem linked with the mesh can be naturally skipped. For example, this is the case for some Particle Vortex Methods like the Diffused Vortex Hydrodynamics (DVH) (Rossi et al., 2015) where BEM and the particle representation of the flow field are coupled together. However, such kind of model has other difficulties such as the modelling of free-surface flows or multi-phase flows for which dedicated algorithms are needed for managing the evolution of those interfaces.

Recently, Eulerian Computational Fluid Dynamics (CFD) solvers, coupled with an Immersed Boundary Method (IBM), have been successful in solving fluid-solid interactions, see Yang et al. (2008) and Yang and Stern (2012). The structure motion is solved in a Lagrangian way while the fluid evolution is solved from an Eulerian point of view. The IBM takes into account how the surface of the solid bodies intersects with the cells where the flow equations are solved. The main drawback of such approach is the need of Adaptive Mesh Refinement (AMR) algorithm in order to use different spatial resolutions for reducing the CPU costs. The AMR techniques require special treatments when writing the code using parallel paradigms. Further,

for these mesh-based methods the treatment of discontinuous interfaces has to be performed with dedicated algorithms, such as the Level-Set or Volume-of-Fluid methods.

Conversely, Lagrangian particle methods can treat those interfaces in a more natural way, see Sun et al. (2018c). On the other hand, as pointed out in Sun et al. (2016), another inherent limitation of Eulerian methods is the lack of the fluid particle trajectories which can be very helpful for the Lagrangian flow feature analysis. Eulerian solvers require the employment of Lagrangian tracers to interpolate their velocities and obtain trajectories in time domain to detect Lagrangian Coherent Structures (LCSs). In contrast, for the Lagrangian particle model, the fluid trajectories are explicitly tracked and therefore it offers special convenience for the analysis of Lagrangian flow features. An example is the use of Finite Time Lyapunov Exponents (FTLEs) which can be evaluated with the relation between the initial and present particle positions. In the present work the ridges of the FTLE field are used to evaluate LCSs for improving the analysis of some of the treated VIV problems.

Smoothed particle hydrodynamics (SPH) method is a Lagrangian particle model which has been rapidly developed for decades and widely applied in different hydrodynamic problems, see Monaghan (2005); Liu and Liu (2010); Shadloo et al. (2016); Zhang et al. (2017); Falahaty et al. (2018) and Liu and Zhang (2019). SPH is a quite robust method in dealing with problems involving moving boundaries, free surface, and material fragmentation, see Marrone et al. (2011b); Liu et al. (2014); Liang et al. (2017) and Zhang and Liu (2018). Recently, SPH has also been widely applied to problems involving flows around bluff bodies, see Shadloo et al. (2011); Ellero and Adams (2011); Sun et al. (2018b) and Zhang et al. (2019). Therefore, with SPH one should be able to solve VIV problems with large-amplitude structure motions and complex boundary conditions. However, considering the state-of-art of SPH, there are several limitations like:

(i) the tensile instability in low-pressure regions;

(ii) numerical high-frequency noise of pressure and velocity-gradient fields;

(iii) high computational costs,

which restrain the range of applicability of the SPH method in the context of VIV problems.

In this paper, it is shown that enhanced versions of the SPH method recently developed can overcome the above drawbacks. In particular we show that the δ^+-SPH model proposed by Sun et al. (2017) can accurately solve some basic but challenging VIV benchmark problems.

Generally VIV problems are defined in free-stream conditions, such as the current flowing around deep-water risers or pylons, the wind passing across long bridges or high-rise buildings, etc. In the modelling of these phenomena, a large fluid domain is required to mimic the free-stream condition and a sufficient long duration is usually requested to monitor the long-time structural response. On the other hand, the Reynolds numbers of these problems are quite high and, to correctly evaluate the shear stress in the thin boundary layer regions, the particle resolution needs to be high enough. The above two conditions require the use of variable spatial resolutions in order to reduce the CPU costs. For this reason the Adaptive Particle Refinement (APR) developed by Chiron et al. (2018b) has been implemented in our SPH solver. For the APR techniques different algorithms have been proposed in the literature, such as Vacondio et al. (2013), Barcarolo et al. (2014) and Tanaka et al. (2018). In the one proposed by Chiron et al. (2018b), an overlapping particle technique has been applied using a parameter interpolation which allows the exchange of the flow information between the different layers of particles (each one with a different particle resolution).

As pointed out by Antuono et al. (2014), a low level of the particle disorder is crucial for an accurate SPH simulation. In SPH, the Naiver-Stokes equations are solved based on the particle approximation whose numerical error is significantly reduced under the condition of a regularized particle distribution. In the boundary layer region, because of the large velocity gradient, the distortion of the particle distributions can be more accentuated with respect to other parts of the fluid domain. Due to these reasons, a Particle Shifting Technique (PST) (Lind et al., 2012) has to be implemented. For example, in Sun et al. (2016) and Sun et al. (2017) it is shown that thanks to the use of a PST the evaluation of velocity gradients in SPH can be largely improved.

Furthermore, PST was shown to be effective in preventing Tensile Instability (TI) by Sun et al. (2017). However, in some cases with strong negative pressure, a more robust way to prevent the occurrence of TI has to be implemented as shown in Sun et al. (2018a).

A robust algorithm for the fluid-rigid bodies coupling is considered in

this paper based on the Fixed Ghost Particles (Marrone et al., 2011b) to update the structure positions whose surfaces serve as boundaries for the fluid evolution. In such kind of simulations difficulties usually arise in three situations:

(i) Firstly, when the mass of the structure is very small, the numerical stability is tightly restricted by the Fluid-Structure-Interaction (FSI) coupling algorithm. As stated in Yang et al. (2008), only when a strong coupling algorithm is implemented the model can simulate problems with a low mass ratio;

(ii) The second difficulty is when the damping ratio is small, which implies a large amplitude of the structural motion. Here the APR technique refines the particles following the movement of the body, and therefore ensures a dynamic particle refinement regardless of the body motion amplitude;

(iii) The last difficulty lies in the number of structures to be modelled. The present fluid-solid coupling algorithm is formulated in a quite general condition allowing for multi-body FSI problems.

Lastly, robust inflow and outflow boundary condition implementations are also important. In addition to the implementation of the open flow boundaries proposed in Federico et al. (2012), the most tough problem arises when strong vortices are transported across the outflow boundary. Indeed, upstream velocities induced by a strong vortex can lead to serious numerical instabilities. To overcome such conditions, in this work a viscous damping buffer zone has been implemented. It results in an increase of the viscosity in the neighbourhood of the outlet section. This damping buffer zone dissipates the vortices ensuring an almost uniform flow velocity pointing outward the outlet. In Section 3 strong vortical flows will be shown thanks to the damping buffer zone which is effective in maintaining the stability at the outlet.

The present article is arranged as follows:

- Section 2 is dedicated to the introduction of the adopted δ^+-SPH model and its related numerical techniques including the boundary implementation, the fluid-solid algorithm, etc.

- Extensive validation is provided in Section 3 through the use of different test-cases for which reference solutions are available in literature.

Thanks to the Lagrangian nature of the SPH, FTLEs are also evaluated in order to highlight the complex flow features in the wake region.

2. Numerical model

2.1. The δ^+-SPH scheme

The recently developed δ^+-SPH model is an enhanced weakly compressible SPH model in which a density diffusive term is added in the continuum equation and a particle shifting technique is nested in the particle motion equation (Sun et al., 2017). Besides that, in the present paper, the Tensile Instability Control (TIC) is applied in the momentum equation by switching the pressure gradient to a non-conservative formulation in the fluid regions characterized by negative pressure, in order to prevent numerical instabilities, see more in Sun et al. (2018a). The governing equations are written as follows:

$$\begin{cases} \dfrac{\mathrm{d}\rho_i}{\mathrm{d}t} &= -\rho_i \sum_j (\boldsymbol{u}_j - \boldsymbol{u}_i)\cdot\nabla_i W_{ij}\, V_j \;+\; \delta\, h\, c_0 \sum_j \mathcal{D}_{ij}\cdot\nabla_i W_{ij}\, V_j, \\ \rho_i \dfrac{\mathrm{d}\boldsymbol{u}_i}{\mathrm{d}t} &= \rho_i\, \boldsymbol{f}_i \;-\; \sum_j \mathcal{F}(p_j, p_i)\,\nabla_i W_{ij}\, V_j \;+\; \mu \sum_j \pi_{ij}\,\nabla_i W_{ij}\, V_j\,, \\ \dfrac{\mathrm{d}\boldsymbol{r}_i}{\mathrm{d}t} &= \boldsymbol{u}_i\,, \qquad p_i \;=\; c_0^2\,(\rho_i - \rho_0)\;, \qquad \boldsymbol{r}_i^* \;=\; \boldsymbol{r}_i \;+\; \delta \boldsymbol{r}_i\,, \end{cases} \tag{1}$$

where ρ_i, $\boldsymbol{u}_i$ and $\boldsymbol{r}_i$ denote the density, velocity and position of the i-th particle, respectively, while, μ is the dynamic viscosity of the fluid, ρ_0 its density at rest condition and $\boldsymbol{f}$ is a generic body-force field. The mass m_i of each particle is imposed as a constant value during the simualtion, and the particle volume is evaluated as $V(t) = m/\rho(t)$. $W_{ij} = W(\boldsymbol{r_i} - \boldsymbol{r_i}, h)$ denotes the kernel function evaluated between particle i and j. In the present work, the C2 Wendland kernel (Wendland, 1995) is adopted and the smoothing length h is set as $h = 2\Delta x$ where Δx is the initial particle spacing. $\nabla_i W_{ij}$ represents the gradient of the kernel function with respect to the position of particle i.

In the weakly compressible SPH model, pressure p is evaluated through the equation of state, in which c_0 is the artificial sound speed which is usually obtained through

$$c_0 \;\geq\; 10\max\Big(U_{max}, \sqrt{p_{max}/\rho_0}\Big)\;, \tag{2}$$

where U_{max} and p_{max} are the maximum expected velocity and pressure. In the present work, U_{max} is set equal to the inflow velocity of the free stream U, and p_{max} is approximated as $1/2\rho_0 U^2$ where ρ_0 is the reference density when the particle pressure is zero. In this way, the density variation of the fluid is limited within 1% of the reference density ρ_0 satisfying the hypothesis of weak-compressibility (Sun et al., 2017).

In the first equation of the system (1), the last term is a density diffusive term which is included to prevent high-frequency instabilities in the density field and therefore the pressure field, being density and pressure linked with the equation of state. As shown in Antuono et al. (2012), δ is a parameter whose optimal value is 0.1, as used in all the simulations of the present work. According to Antuono et al. (2010), the diffusive term $\mathcal{D}_{ij}$ is written as:

$$\mathcal{D}_{ij} = 2\left[(\rho_j - \rho_i) - \frac{1}{2}\left(\langle\nabla\rho\rangle_i^L + \langle\nabla\rho\rangle_j^L\right)\cdot\boldsymbol{r}_{ji}\right]\frac{\boldsymbol{r}_{ji}}{\|\boldsymbol{r}_{ji}\|^2}, \tag{3}$$

where $\boldsymbol{r}_{ji} = \boldsymbol{r}_j - \boldsymbol{r}_i$ and $\langle\nabla\rangle^L$ is the renormalized spatial gradient, see for details in Antuono et al. (2010). The terms related to the density gradients contribute to improving the accuracy and consistency in the free-surface region where the kernel function is truncated. In addition, it also helps to reduce the numerical dissipation in the whole flow field, see Antuono et al. (2015).

In the second equation of the system (1), $\boldsymbol{f}$ is a generic body force field, while the last term is the viscous force, where μ denotes the dynamic viscosity. The viscous term is represented following Monaghan and Gingold (1983), where π_{ij} is written as:

$$\pi_{ij} = 2(d+2)\frac{(\boldsymbol{u}_j - \boldsymbol{u}_i)\cdot\boldsymbol{r}_{ji}}{\|\boldsymbol{r}_{ji}\|^2}, \tag{4}$$

where d is the spacial dimension of the problem.

Regarding the pressure force, a novel treatment for the pressure gradient $\mathcal{F}_{ji} = \mathcal{F}(p_j, p_i)$ is introduced. Generally, in the traditional weakly-compressibility SPH models, this term is represented by the sum $(p_j + p_i)$. However, as highlighted in Sun et al. (2018a), differential operators can be adopted in the following manner in order to completely prevent the occurrence of Tensile Instability:

$$\mathcal{F}_{ji} = \begin{cases} p_j + p_i & p_i \geq 0 \quad \text{or} \quad i \in \mathscr{S}_F, \\ p_j - p_i & p_i < 0 \quad \text{and} \quad i \notin \mathscr{S}_F, \end{cases} \tag{5}$$

where $\mathscr{S}_F$ denotes the particles belonging to the free-surface and their neighbour particles, see more in Sun et al. (2017). The use of $\mathscr{S}_F$ in (5) is crucial to enforce correctly the dynamic boundary condition on the free-surface, see Colagrossi et al. (2009) and Colagrossi et al. (2011). The free surface particles are detected through the algorithm described in Marrone et al. (2010). In addition, as validated in Sun et al. (2018a), Eq. (5) is effective in preventing the occurrence of Tensile Instability for both two and three dimensional viscous flows around bluff bodies, even at much higher Reynolds numbers.

The non-conservative pressure gradient leads to errors in the momentum conservation when the particle distribution becomes irregular. Therefore a Particle Shifting Technique (Lind et al., 2012; Sun et al., 2017; Khayyer et al., 2017) is nested into the formulation of the particle motion. The shifting vector is given by:

$$\delta \boldsymbol{r}_i \;=\; -\,CFL\,\frac{U_{max}}{c_0}\,(2h_i)^2 \sum_j \left[\,1 \;+\; R\left(\frac{W_{ij}}{W(\Delta x_i)}\right)^n\,\right] \nabla_i W_{ij}\,\frac{m_j}{\rho_i+\rho_j}\,, \qquad (6)$$

where, according to Sun et al. (2017), $n = 4$, $R = 0.2$ and CFL is the Courant-Friedrichs-Levy number (here set equal to 1.5). The amplitude of the particle shifting $|\delta \boldsymbol{r}_i|$ is always a small fraction of the particle size Δx_i. And it has been recently confirmed in Sun et al. (2019) that, as the particle resolution increases, $|\delta \boldsymbol{r}_i|/\Delta x_i$ tends to zero.

A fourth-order Runge-Kutta scheme is used to march in time the system (1). As described in Sun et al. (2017), in order to reduce CPU costs and improve the stability of the scheme, the particle repositioning is applied outside the sub-time steps of the Runge-Kutta scheme.

The time step of the simulations is set as:

$$\Delta t \;=\; \min(\Delta t_c, \Delta t_v)\,, \qquad \Delta t_c = 3\,h/c_0\,, \quad \Delta t_v \;=\; 0.125h^2/\nu\,, \qquad (7)$$

where Δt_c and Δt_v are the time step due to the acoustic and viscous constraints (see *e.g.* Colagrossi et al. (2016)). In the simulations presented in this article the acoustic constraint is always the most restrictive one (i.e. $\Delta t_c < \Delta t_v$).

2.2. Boundary conditions

For the simulations in this work, three different boundary conditions are involved. They are respectively the free-slip wall boundary for modelling

the lateral channel walls, the no-slip wall boundary for the surface of the moving bodies and inflow and outflow boundaries for modelling the free stream condition. The former two wall boundaries are implemented using the Fixed Ghost Particles as proposed in Marrone et al. (2011b) and the last ones are adopted similar to the inlet and outlet boundaries of the open channel flows as introduced by Federico et al. (2012).

Regarding the inlet boundary, particles with a certain inflow velocity are arranged on the left side of the inlet with a width equal to the kernel radius. Once an inlet particle is transported across the left border of the flow region, it is switched into a normal fluid particle and a new inlet particle is generated at a distance of Δx to the left of the leftmost inlet particle. We note that the inflow velocity can be either uniform to model a free-stream or varied in the vertical direction to model a shear flow. Regarding the outlet boundary, the fluid particles which cross the right border of the flow region will be switched to frozen particles whose density derivatives are zero, but their velocities and motions are still updated by the momentum and motion equations. The width of the outlet buffer zone (occupied by frozen particles) has to be larger than the radius of the kernel function, as in the inlet region. From the numerical point of view the frozen particles which are transported outside the outlet buffer zone will be recycled to be reused in the inlet.

However, for the specifics of the test-cases solved in this work, we underline that the outlet boundary has to be applied along with a damping zone with a width of 2L (where L is the characteristic length of the immersed bluff body), in order to damp the strong vortex structures shed by the solid body which can induce strong back-flows across the outlet buffer zone (Sun et al., 2018a). In all the test cases of the present work the viscosity coefficient in the damping region is increased to obtain the highest Reynolds number,$\mathrm{Re}^{\star}$ allows by the time step Δt_c of eq. (7). It follows that $\mathrm{Re}^{\star}$ is $\mathcal{O}(10)$ for the simulations presented in this work.

Other possible algorithms for modelling inlet and outlet boundary condition with SPH can be found in Lastiwka et al. (2009), Kazemi et al. (2017) and Tafuni et al. (2018).

2.3. Coupling algorithm for the fluid-solid interaction

In this subsection, the coupling algorithm for the fluid-solid interaction is presented. In this work the structure is regarded as rigid body without considering the structural deformation. Generally, two kinds of reference frames, respectively earth-fixed (inertial) and body-fixed (non-inertial)

reference frames, are involved. The fluid evolution is solved in the earth-fixed reference frame, while the body motions induced by the hydrodynamic forces are updated through the Euler angles linking the earth-fixed and body-fixed reference frames. We note that the origin of coordinates of the body-fixed frame locates at the body's mass-center which is denoted by subscript O in the earth-fixed frame and subscript O' in the body fixed frame.

As stated in the last section, Fixed Ghost Particles are used inside the solid bodies. Following Bouscasse et al. (2013), the dynamical state of these particles is expressed through the vector:

$$\boldsymbol{y}_g = (..., \rho_j, p_j, \boldsymbol{u}_j, \boldsymbol{r}_j, ...) \qquad j \in \text{index of ghost particles}, \tag{8}$$

$\boldsymbol{y}_g$ serves for the enforcement of the boundary conditions for fluid particle system.

Similarly, the dynamic state of fluid particles can be expressed through the vectors $\boldsymbol{y}_f$ as follows:

$$\boldsymbol{y}_f = (..., \rho_i, p_i, \boldsymbol{a}_i, \boldsymbol{u}_i, \boldsymbol{r}_i, ...) \quad i \in \text{index of fluid particles}. \tag{9}$$

where $\boldsymbol{a}_i$ denotes the particles' acceleration given by (1). In $\boldsymbol{y}_g$ and $\boldsymbol{y}_f$, the coordinates of the quantities are all expressed in the earth-fixed frame.

The translational motion of the rigid body is updated by the position, velocity and acceleration of the body mass-center namely: $\boldsymbol{d_O}$, $\boldsymbol{U_O}$, $\dot{\boldsymbol{U}}_{\boldsymbol{O}}$. Since in the present work the simulations are carried out in two dimensions the rotational motion is updated through the angle $\theta(t)$. However, for the sake of completeness, the general rigid body dynamics in a three-dimensional framework is reported in Appendix A. The variables for updating the body position and orientation can be summarized as

$$\boldsymbol{y}_b = \left(\dot{\boldsymbol{U}}_{\boldsymbol{O}}, \boldsymbol{U_O}, \boldsymbol{d_O}, \ddot{\theta}, \dot{\theta}, \theta, ..., \boldsymbol{a}_j^b, \boldsymbol{u}_j^b, \boldsymbol{r}_j^b, ...\right), \tag{10}$$

where $\boldsymbol{a}_j^b, \boldsymbol{u}_j^b$ and $\boldsymbol{r}_j^b$ are the acceleration, velocity and position of the nodes used to discretize the body surface, respectively.

The governing equations for the translational and rotational accelerations of the rigid bodies can be written in 2D as:

$$\begin{cases} M\dot{\boldsymbol{U}}_{\boldsymbol{O}} = \boldsymbol{F_O} + M\boldsymbol{g}, \\ I_O\,\ddot{\theta} = \boldsymbol{T_O} \cdot \boldsymbol{e}_3, \end{cases} \tag{11}$$

where M is the body mass and I_O the moment of inertia with respect to the mass center and $\boldsymbol{e}_3$ the normal vector to the 2D flow plane. The hydrodynamic force $\boldsymbol{F_O}$ and torque $\boldsymbol{T_O}$ on the rigid body are obtained through the balance of interacting forces between the fluid particles (indexed by i) and fixed ghost particles (indexed by j):

$$\begin{cases} \boldsymbol{F_O} = -\sum_i \sum_j \left[-(p_j + p_i) + \mu\pi_{ij} \right] \nabla_i W_{ij} V_i V_j, \\ \boldsymbol{T_O} = -\sum_i \sum_j \left(\dfrac{\boldsymbol{r}_i + \boldsymbol{r}_j}{2} - \boldsymbol{d_O} \right) \times \left[-(p_j + p_i) + \mu\pi_{ij} \right] \nabla_i W_{ij} V_i V_j. \end{cases} \tag{12}$$

In Eqs.(12), the pressure p_j and velocity $\boldsymbol{u}_j$ for the ghost particles are interpolated from fluid particles satisfying the non-penetration and no-slip boundary conditions, see more details in Bouscasse et al. (2013).

Once the body accelerations are evaluated through Eqs.(11) the accelerations, velocities and positions of the solid surface nodes can be updated with:

$$\begin{cases} \boldsymbol{a}_j = \dot{\boldsymbol{U}}_{\boldsymbol{O}} + \dot{\boldsymbol{\omega}} \times \boldsymbol{r}_j + \boldsymbol{\omega} \times (\boldsymbol{\omega} \times \boldsymbol{r}_j) \\ \boldsymbol{u}_j = \boldsymbol{U_O} + \boldsymbol{\omega} \times \boldsymbol{r}_j, \\ \boldsymbol{r}_j = \boldsymbol{d_O} + \mathbb{R}_\theta \, \boldsymbol{r'}_j, \end{cases} \tag{13}$$

where the angular velocity vector is $\boldsymbol{\omega} = \dot{\theta}\boldsymbol{e}_3$. $\boldsymbol{r}'_j$ is the vector representing the coordinate of particle/node j in the body-fixed frame. The matrix $\mathbb{R}_\theta$ is the rotation matrix:

$$\mathbb{R}_\theta = \begin{bmatrix} \cos\theta & -\sin\theta & 0 \\ \sin\theta & \cos\theta & 0 \\ 0 & 0 & 1 \end{bmatrix} \tag{14}$$

which is used together with $\boldsymbol{d_O}$ to update the position of the ghost particles. Eqs.(13) are then used in the extrapolation process for determining the velocity and pressure of the fixed ghost particles, see more in Marrone et al. (2011a). Once the fixed ghost particles are updated with the above equations, the fluid particles accelerations, Eqs.(1), can be evaluated.

The mutual interaction between fluid and fixed-ghost particles has been analysed in Cercos-Pita et al. (2017) demonstrating the consistency of such kind of approach within the SPH model.

In the proposed method, the movements of the fluid particles, Eqs.(1), and the motions of the rigid body, Eqs.(11), are solved simultaneously using a 4^{th} order Rung-Kutta time integration. This is because the fluid evolution and the rigid motion are both processed in an explicit manner in the same framework and the time step is very small as restricted by the sound speed. The stability of the proposed scheme allows even to simulate problems with a density ratio between the rigid body and the surrounding fluid less than one. Indeed the latter condition implies that the added mass force components become relevant and this generally requires particular care for time integrations of fluid-solid coupled dynamics as commented also in Bouscasse et al. (2013).

2.4. Adaptive Particle Refinement

In order to well resolve the shear stress in the boundary layer, a sufficient particle resolution has to be imposed near the body surface. While as stated before, most VIV problems are modelled in free stream condition which means a large computational domain is needed. In that case, if the fluid domain is discretized with a unified particle resolution, it will inevitably lead to huge particle numbers. For this reason the Adaptive Particle Refinement (APR) algorithm described in Chiron et al. (2018b) is used in the present work. The latter consists in a subdivision of the fluid domain in regions of different spatial resolutions. The more refined subdomains are the ones close to solid bodies and move according to them.

3. Numerical results

In this section, a number of test-cases of VIV problems are presented in order to validate the proposed δ^+-SPH model. As a comprehensive validation, different aspects of the SPH results, including the force coefficients measured on cylinders, the body's VIV trajectories and the shapes of vortex streets behind the cylinder are compared against experimental data or other numerical results available from the literature.

In the following text the drag and lift force coefficients are denoted as C_D and C_L and defined as:

$$C_D = \frac{f_D}{\frac{1}{2}\rho U^2 D}; \quad C_L = \frac{f_L}{\frac{1}{2}\rho U^2 D}, \tag{15}$$

where f_D and f_L are the horizontal and vertical components of the force $\boldsymbol{F_O}$ evaluated through the first formula in Eqs. (12).

In the following subsections, six benchmark test-cases with increasing complexity are considered:

I) The first validation starts from a case involving a free-stream flow around a fixed cylinder and the force coefficients on the cylinder are validated;

II) The second test is the viscous flow around a forced oscillating cylinder and different modes of vortex wakes are compared against experimental observations;

III) In the third benchmark test, transverse galloping of a rectangular box on an elastic support is modelled and a convergence test has been conducted to investigate the effect of particle resolutions;

IV) In order to test the accuracy of the fluid-solid coupling algorithm, vortex induced vibrations of circular cylinders with very small mass ratios are then investigated in the fourth benchmark test. Validations are carried out by comparing the SPH results against the reference solutions in terms of the force components and the vibrating trajectory of the cylinder;

V) In the fifth benchmark test, rotational galloping motions of a rectangular box with two damping ratios, under which the maximum rotation angle can be less or larger than 90 degrees, are modelled. The fluid-solid system solved in two dimensions allows an arbitrary rotation of the rectangular body;

VI) The last benchmark case considers two galloping bodies, the coupling interactions between them are modelled and validated. In addition, the interacting mechanism between the two bodies is analysed by using LCSs to reveal the Lagrangian flow features.

3.1. Flow past a stationary circular cylinder

In this subsection, a test-case of the flow past a stationary circular cylinder at Reynolds number Re=200 is conducted for a primary validation of the δ^+SPH scheme. The simulation is conducted in the fluid domain with the size of $[-10D, 30D] \times [-10D, 10D]$ where D is the cylinder diameter and the center of the cylinder is located at the origin of the reference frame.

Firstly, a convergence study is conducted for determining the required particle resolution in the nearfield of the cylinder. Three different particle resolutions as $D/\Delta x = 25$, $D/\Delta x = 50$ and $D/\Delta x = 100$ are used close to the cylinder. In the three cases, the particle resolutions in the far field are all de-refined to $D/\Delta x = 12.5$ for reducing the entire computational cost. Time evolutions of the drag and lift force coefficients with the three particle refinements are plotted in Figure 1. As the particles in the near field are refined, the forces converge gradually. Based on the average drag force coefficients, the convergence rate is evaluated as $r_c \simeq 1.58$ which is calculated with $\log(\epsilon_{21}/\epsilon_{32})/\log(2)$ where ϵ_{21} indicates the absolute error between the drag force coefficients obtained with $D/\Delta x = 50$ and $D/\Delta x = 25$ and ϵ_{32} denotes the absolute error between $D/\Delta x = 100$ and $D/\Delta x = 50$.

With the finest particle resolution of $D/\Delta x = 100$, the vorticity field in the flow behind the cylinder is depicted in Figure 2. Classic Von Karman vortex street is observed behind the cylinder. Although the particles in the far

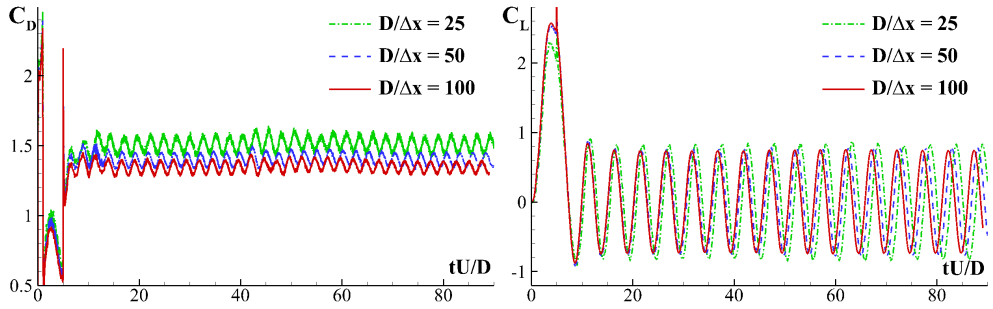

Figure 1: Time evolutions of the drag and lift force coefficients in the free-stream flow past a fixed circular cylinder at $Re = 200$; the SPH results of three particle resolutions as $D/\Delta x = 25$, $D/\Delta x = 50$ and $D/\Delta x = 100$ are compared.

Table 1: Drag and lift coefficients in the free stream flow past a fixed circular cylinder at $Re = 200$.

	Drag coefficient C_D	Lift coefficient C_L
Liu et al. (1998)	1.31 ± 0.049	± 0.69
Braza et al. (1986)	1.40 ± 0.05	± 0.75
Ng et al. (2009)	1.373 ± 0.050	± 0.724
DVH (Rossi et al., 2015)	1.354 ± 0.050	± 0.680
The present δ^+-SPH	1.345 ± 0.050	± 0.732

field have been de-refined into a rough resolution, the continuity and stability of the vorticity field are still maintained at the particle splitting interface. The drag and lift force coefficients are plotted in Figure 3, comparing against the results by DVH from Rossi et al. (2015). As shown in Table 1, the force coefficients C_D and C_L solved by the δ^+-SPH model agree fairly well with the reference results from the literature. The reference solutions are all obtained with numerical models. Indeed at Re=200 three-dimensional instabilities take place in experiments and therefore cannot be used for the validation.

3.2. Flow past a forced oscillating circular cylinder

The classic Von Karman vortex street describes the shape of the vortex structure shed from a fixed body. In the case of flow past an oscillating body, the vortex street can be quite different and the latter has been experimentally and numerically studied in the literature, see Meneghini and Bearman (1995).

Different wake patterns induced by the cylinder motions were observed. As found by Meneghini and Bearman (1995), when the oscillating amplitude of the body exceeds a certain value, the vortical wake becomes asymmetric, evolves from a so-called **2S mode** (two single vortices shed in one period) to a **P+S mode** (one pair and one single vortex shed in one period), which can be observed in the experimental dye visualizations, see Williamson and Govardhan (2004). In the numerical results by Eulerian CFD solvers, vorticity fields evaluated from the velocity gradient as an Eulerian description are usually depicted to show the wake patterns (Deng et al., 2007), while in

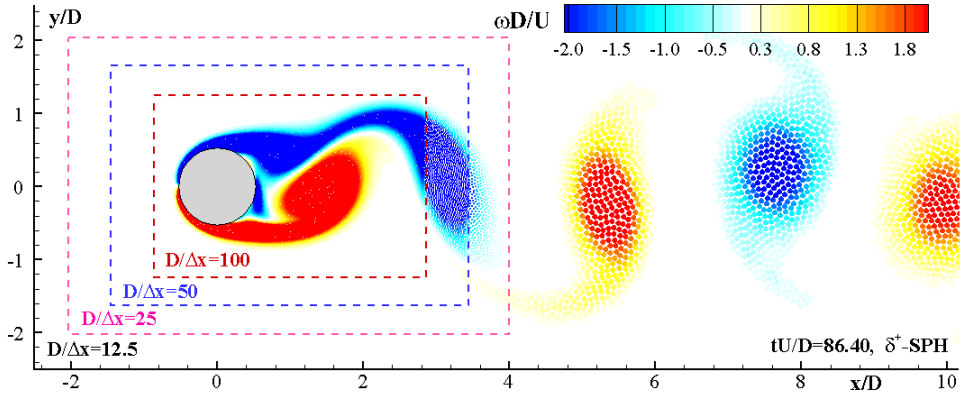

Figure 2: The vorticity field in the free stream flow past a fixed circular cylinder at $Re = 200$.

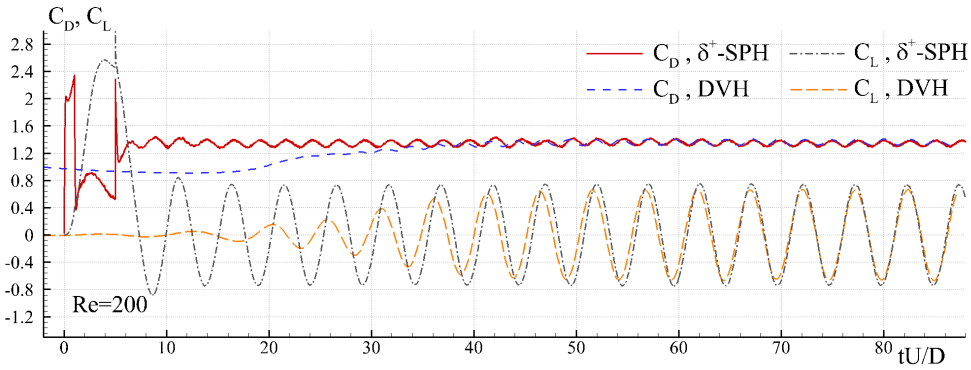

Figure 3: Time evolution of the drag and lift force coefficients in the free-stream flow past a fixed circular cylinder at $Re = 200$.

Table 2: Parameters for the test-cases of flow past a forced oscillating circular cylinder.

Test case number	Oscillating frequency f	Oscillating amplitude A_y
1	$0.8f_s$	$0.55D$
2	$0.8f_s$	$0.60D$
3	$0.8f_s$	$0.65D$

this subsection, thanks to the explicit tracking of the particle trajectories in the SPH results, Lagrangian Coherent Structures (LCSs) have been detected directly through the ridges of FTLE field to show the vortical flow features, see Sun et al. (2016). The shape of LCSs resembles the experimentally observed vortex street, supplies a new way for the study of vortex wakes in VIV problems. In the following, three test-cases of the flow past a forced oscillating circular cylinder at Reynolds number $Re = 200$ are carried out. The size of the fluid domain is the same as the one in Section 3.1 but 3 levels of particle resolutions are adopted here so that we have $D/\Delta x = 100$ on the cylinder surface and $D/\Delta x = 25$ in the far field. Parameters describing the cylinder motions of the three tests are summarized in Table 2 where $f_s = 0.196U/D$ is the vortex shedding frequency of the flow past a fixed circular cylinder at the same Reynolds number, see Section 3.1. In these cases, $X = x/D$ and $Y = y/D$ denote the dimensionless position of the cylinder in the horizontal and transverse directions. X is fixed to zero while the transverse position Y is updated with the vertical acceleration as

$$\ddot{Y} = -(2\pi f)^2 A_y \cdot \cos(2\pi f t), \tag{16}$$

where f denotes the oscillating frequency and A_y stands for the oscillating amplitude. Integrating Eq. (16) in time, the transverse velocity and position of the cylinder can be updated in each time step. The δ^+SPH results show that, as A_y is increased from $0.55D$ to $0.6D$, the vortex shedding evolves from the **2S mode** to the **P+S mode** (see the plots in Figure 4). A good agreement is obtained between the SPH results and the experimental snapshots provided by Williamson and Govardhan (2004). If we further increase A_y to $0.65D$, the size of the single vortex in the **P+S mode** is enlarged, as shown in Figure 5 where our SPH result agrees well with an Immersed Boundary Method (IBM) solution by Deng et al. (2007).

3.3. Vortex induced transverse vibration of a rectangular body

Conversely to the previous case, in this subsection the vortex induced motions of a cylinder with rectangular cross section is considered. The side length ratio of the rectangular body is $L/D = 1.5$, where L and D denote the horizontal length and vertical height, respectively. Due to the transverse force induced by the vortex shedding, the rectangular body can oscillate in the transverse direction restricted by an elastic support while the in-line and rotational motions are blocked. The Reynolds number with respect to the reference length D is set equal to Re=250.

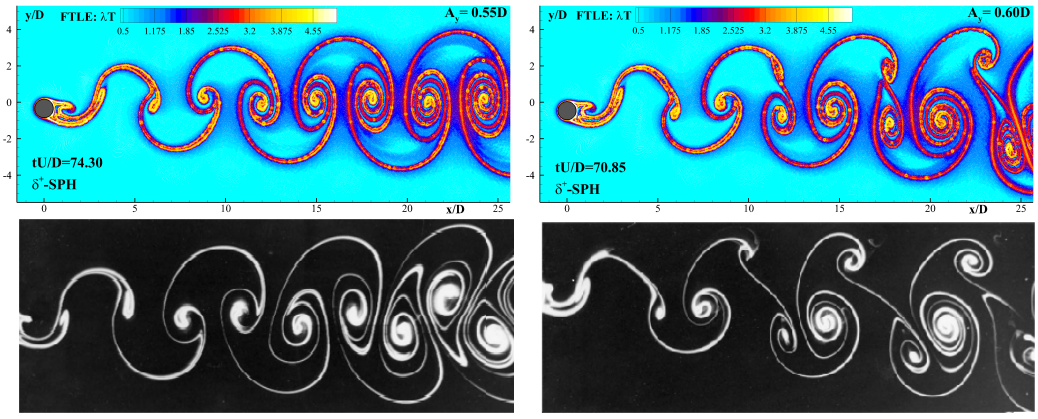

Figure 4: The vortex street behind the oscillating cylinder. The δ^+SPH results (top panels) are compared to experimental dye visualizations from Williamson and Govardhan (2004) (bottom panels). **2S mode** is observed on the left side when $A_y = 0.55D$ and **P+S mode** is observed on the right side when $A_y = 0.60D$.

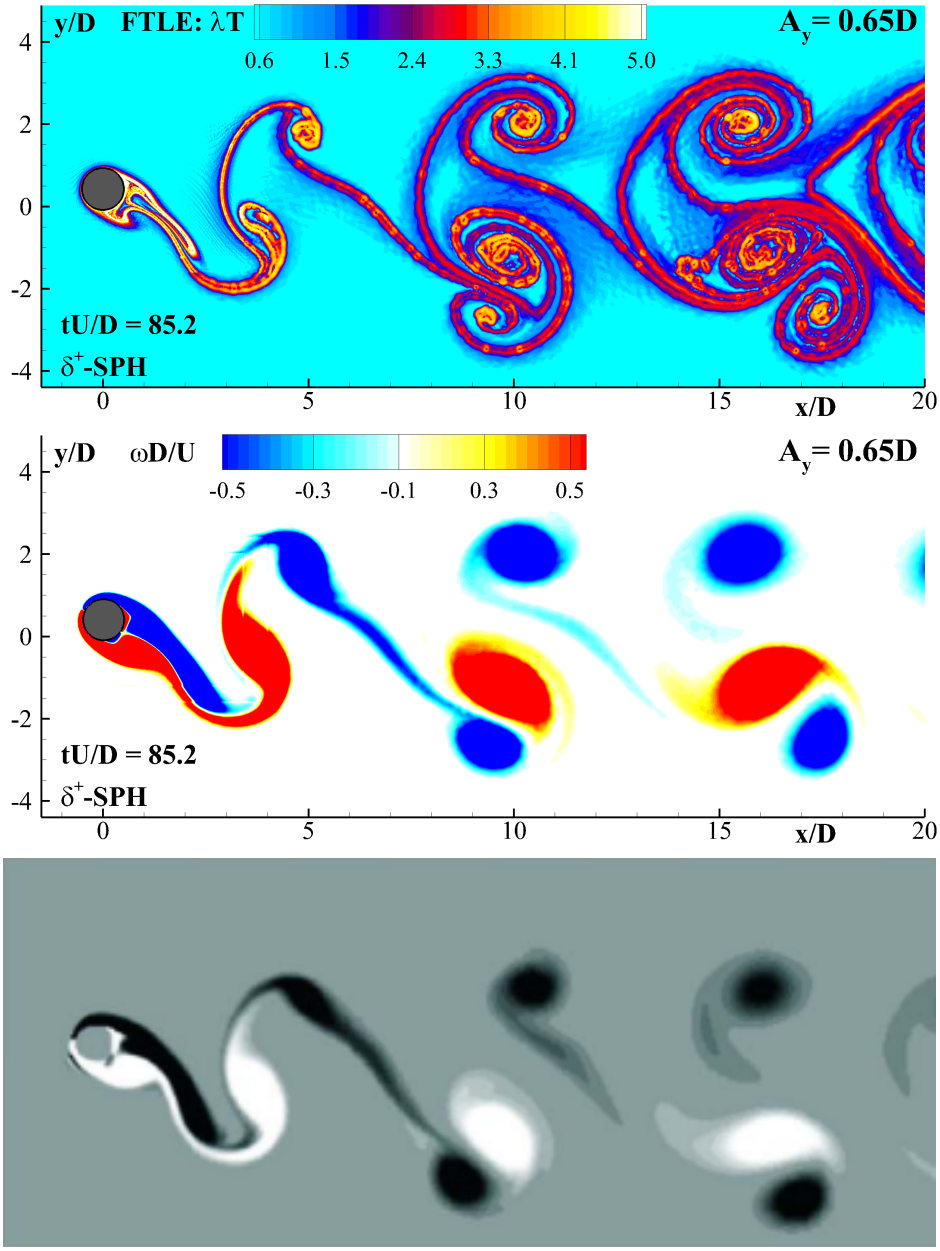

Figure 5: The vortex street behind the cylinder oscillating with the amplitude $A_y = 0.65D$; the top and middle panels show the Lagrangian Coherent Structures and the vorticity field by the δ^+SPH while the bottom panel shows the vorticity field evaluated through an immersed boundary method by Deng et al. (2007).

In these cases, the numerical treatment at the region of sharp corners can introduce further complexities. Special mesh/particle refinements have to be imposed in these regions to capture the boundary layers characterized by high velocity or pressure gradients, see Rossi et al. (2016). In SPH models, this kind of regions consisting of sharp corners usually bring challenges for the implementation of solid wall boundaries. For example, the rapid pressure drop behind the sharp corners can also excite the tensile instability which leads to numerical cavitation. As shown in Sun et al. (2017), the δ^+SPH was developed to tackle these numerical difficulties.

Based on the governing equations (see Eqs. 11) in Section 2.3, the numerical damping has been added for limiting the body-motion amplitude (Robertson et al., 2003). Finally, the governing equation for the box motion in the transverse direction is written as

$$\ddot{Y} + 2\zeta \left(\frac{2\pi}{U^*}\right) \dot{Y} + \left(\frac{2\pi}{U^*}\right)^2 Y = \frac{2C_L}{\pi m^*}\,, \tag{17}$$

where ζ is the damping ratio which is given by $\zeta = c/(2\sqrt{km})$ where c is the damping coefficient, k the spring coefficient and m the mass of the body. $U^* = U/(fD)$ is named as the reduced velocity in which $f = (1/2\pi)\sqrt{k/m}$ is the natural vibration frequency. $m^* = m/m_f$ is the mass ratio in which m_f is the mass of the fluid volume displaced by the body.

In this case, the mass ratio is $m^* = 10$, the reduced velocity is $U^* = 6$, and the damping ratio is $\zeta = 0.0037$. The same case has be modelled by Robertson et al. (2003) through a two-dimensional Spectral Element Method (SEM) whose results will be adopted here as reference for validation.

The simulation is conducted in a free-stream with the size of $[-10D, 30D] \times [-10D, 10D]$ and the center of the cylinder is located at the origin of the reference frame. In the SPH simulation, the finest particle resolution adopted to discretize the rectangular body is $D/\Delta x = 100$ and 3 levels of particle refinements are used in the test of the flow, so that the particle size is increased of 4 times in the far field.

After $t = 40D/U$ seconds the VIV motion reaches a periodic regime. Top plot of Figure 6 depicts the vorticity field of the SEM when the rectangular body reaches the maximum transverse position. Bottom plot of the same figure shows the vorticity field of the δ^+SPH . The two solvers are in a good agreement. Time evolutions of the displacement of the rectangular body in the transverse direction are plotted in Figure 7. As the particle resolution

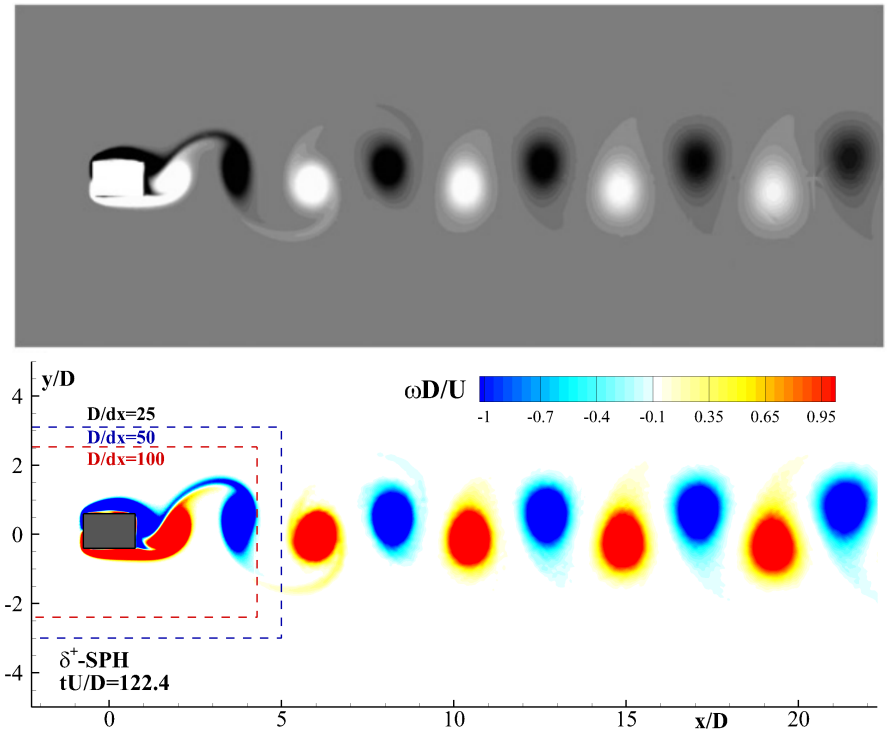

Figure 6: The vorticity field behind the oscillating rectangular body at the maximum transverse motion. The result of Spectral Element Method by Robertson et al. (2003) (top panel) is compared with the present δ^+SPH result (bottom panel).

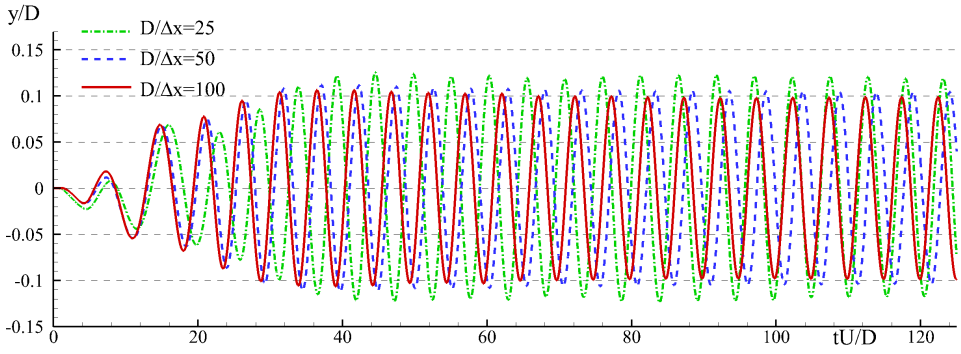

Figure 7: Time evolution of the displacement of the rectangular body in the transverse direction. Results of three different particle resolutions are compared.

for discretizing the rectangular body is refined, the oscillating amplitude is reduced showing a convergence trend.

The amplitude of the transverse motion in the steady stage is summarized in Table 3. The δ^+SPH result with $D/\Delta x = 100$ is very close to the reference solution of Robertson et al. (2003). The convergence rate for the maximum displacement is calculated as $\log(\varepsilon_{32}/\varepsilon_{21})/\log(2) = 1.28$ where ε_{32} indicates the absolute error between the results with $D/\Delta x = 50$ and with $D/\Delta x = 25$ while ε_{21} indicates the absolute error between the results with $D/\Delta x = 100$ and with $D/\Delta x = 50$.

Table 3: Maximum amplitude of transverse galloping of a rectangular box with the parameters: $m^* = 10$, $U^* = 6$ and $\zeta = 0.0037$.

Methods	Maximum galloping amplitude (Y_{max}/D)
SEM by Robertson et al. (2003)	0.095
δ^+SPH with D/$\Delta x = 25$	0.123
δ^+SPH with D/$\Delta x = 50$	0.106
δ^+SPH with D/$\Delta x = 100$	0.099

3.4. Vortex induced streamwise and transverse vibrations of a circular cylinder

In this subsection, vortex induced vibrations of a circular cylinder in both streamwise and transverse directions (denoted as X-Y vibration) are considered. According to Yang et al. (2008), the governing equations with numerical damping for the cylinder motions are written as:

$$\begin{cases} \ddot{X} + 2\zeta_X \left(\dfrac{2\pi}{U_X^*}\right)\dot{X} + \left(\dfrac{2\pi}{U_X^*}\right)^2 X = \dfrac{2C_D}{\pi m^*}, \\ \ddot{Y} + 2\zeta_Y \left(\dfrac{2\pi}{U_Y^*}\right)\dot{Y} + \left(\dfrac{2\pi}{U_Y^*}\right)^2 Y = \dfrac{2C_L}{\pi m^*}, \end{cases} \tag{18}$$

where D is the diameter of the circular cylinder and $X = x/D$ and $Y = y/D$ denote the dimensionless positions of the body in the streamwise and transverse directions. The subscripts using X and Y denote the corresponding parameters in these two directions.

As has been emphasized by Yang et al. (2008) and recently by Jaiman et al. (2016), only a strong FSI coupling algorithm can be applied to model

VIV problems with small mass ratios. In Yang et al. (2008), the weak-coupling algorithm failed when $m^* \leq 1.07$. In Jaiman et al. (2016), the strong staggered coupling (SSC) scheme failed when $m^* = 0.52$. In order to test the performance of the present δ^+SPH scheme different cases with different mass ratios including $m^* \leq 0.52$ are tested and validated.

Firstly, the X-Y vibration of a circular cylinder at $Re = 100$ is modelled. The parameters for the VIV system are set as $m^* = 0.52$, $U_X^* = U_Y^* = 5.0$, and $\zeta_X = \zeta_Y = 0$. The size of the fluid domain in the SPH simulation is $[-10D, 30D] \times [-10D, 10D]$ and the center of the cylinder is located at the origin of the reference frame.

A particle spacing with $D/\Delta x = 100$ is adopted to discretize the circular cylinder and 4 levels of particle refinements are used, so that the particles in the far field have a size eight times higher than close to the body.

The lift force coefficient on the cylinder is measured and compared in Figure 8 against the results of the Nonlinear Interface Force Correction (NIFC) scheme proposed by Jaiman et al. (2016). Excellent agreement between the two solvers is achieved in the steady state. In addition, snapshots of the vorticity fields at the maximum and minimum transverse displacements of the cylinder are depicted in Figure 9. Again, the vorticity distributions between the two solvers agree well with each other.

Trajectories of the cylinder motions are usually plotted for the analysis of VIV problems. For the purpose of a further validation of the SPH scheme, we choose another documented case of a circular cylinder vibrating in cross flow under vortex shedding exciting. The Reynolds number for this case

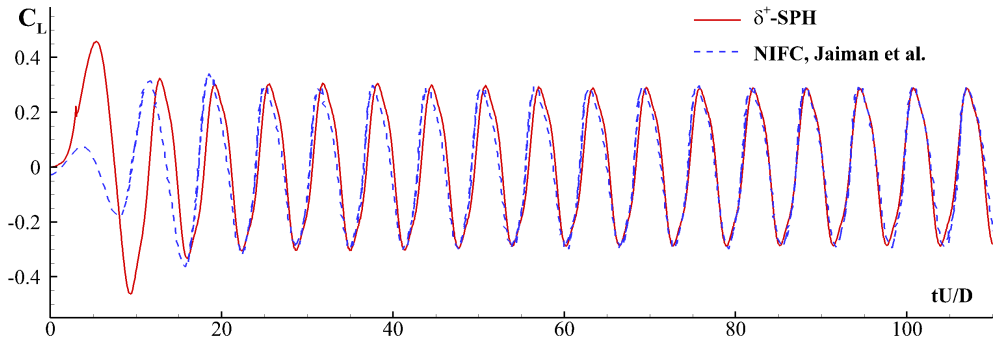

Figure 8: Time evolutions of the lift force coefficient C_L at $Re = 100$, $m^* = 0.52$, $U_X^* = U_Y^* = 5.0$ and $\zeta_X^* = \zeta_Y^* = 0$; the δ^+SPH and the reference solution from Jaiman et al. (2016) are compared.

is increased to Re=200. The cylinder can vibrate in both streamwise and transverse directions under the restriction of the spring support characterized by $U_X = U_Y = 5.0$ and $\zeta_X^* = \zeta_Y^* = 0.01$. Two mass ratios of $m^* = 4/\pi$ and $m^* = 0.5$ are investigated to show the mass ratio effects. It is worth mentioning that by using a weakly coupling algorithm in Yang et al. (2008), the simulation failed when $m^* \leq 1.07$ and the same case can only be modelled using a strong FSI coupling embedded-boundary method. The size of the fluid domain, the initial position of the cylinder and the implementation of the Adaptive Particle Refinement are the same of the previous case at Re=100.

Firstly the vorticity fields at the maximum displacements obtained at two mass ratios are depicted in Figure 10 and the results between the immersed boundary method (Yang and Stern, 2012) and δ^+SPH are compared against each other. Good agreements are obtained.

Numerical instabilities are not observed in the small mass ratio case, $m^* = 0.5$, showing the robustness of the algorithm adopted in the δ^+SPH framework. The trajectories of the cylinder motions are plotted in Figure 11. For the case of $m^* = 4/\pi$, three different reference solutions, respectively from Blackburn and Karniadakis (1993), Étienne and Pelletier (2012) and Yang and Stern (2012), are reported on the left of Figure 11. The SPH results agree well with all of them. The oscillating amplitude of Yang and Stern (2012) is slightly smaller than the other three results. In the case of $m^* = 0.5$,

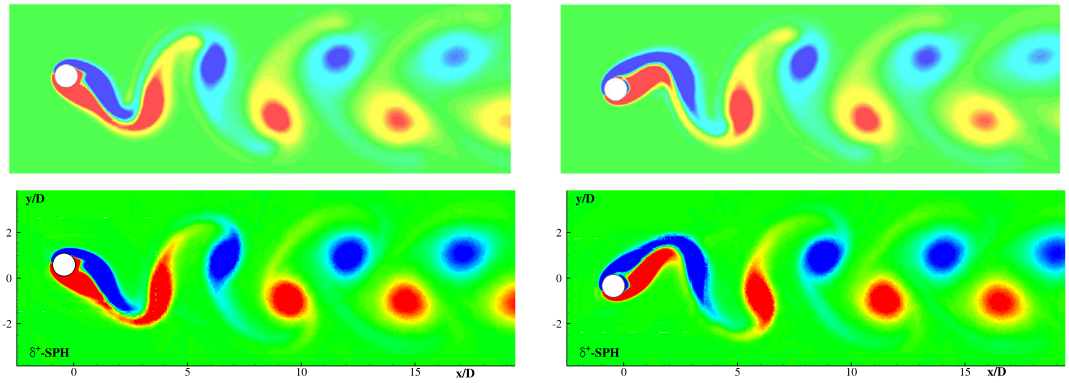

Figure 9: Snapshots of the vorticity fields at the maximum (left) and minimum (right) transverse displacements of the cylinder. Top row: results of the NIFC scheme by Jaiman et al. (2016). Bottom row: δ^+-SPH (bottom panels). Dimensionless vorticity $\omega\, D/U$ scales from -1 (blue) to 1 (red).

since the mass ratio is quite small, only one reference solution is available in the literature (Yang and Stern, 2012). In the right plot of Figure 11, the δ^+SPH result is compared with this solution obtained through a strong FSI coupling scheme using an immersed boundary method. Similar to the previous test, the reference solution is again slightly smaller than the δ^+SPH solution. However, the overall trajectories of the different solutions show a quite similar behaviour. Because of significant reduction of the cylinder mass the discrepancy between the two solvers is larger.

3.5. Vortex induced rotational vibrations of a rectangular body

As a fifth test-case, here, we consider the rotational motion induced on a rectangular body. The latter has the horizontal and vertical motions blocked while the rotation is allowed and counterbalanced by the action of a torsional spring. For this benchmark the Reynolds number is set equal to Re$= UD/\nu = 250$, where U is the free-stream velocity, D the width while the length is $L = 4D$.

The fluid domain is characterized with the size of $[-15D, 45D] \times [-20D, 20D]$ and the center of the rectangular body is located at the origin of the reference frame. The particle distance used for discretizing the body is $\Delta x = D/50$. With the using of 3 levels of particle refinements, the particle size in the far field can be de-refined for the aim of a reduction of the total computational cost. Indeed, in this test case APR contributes to a reduction

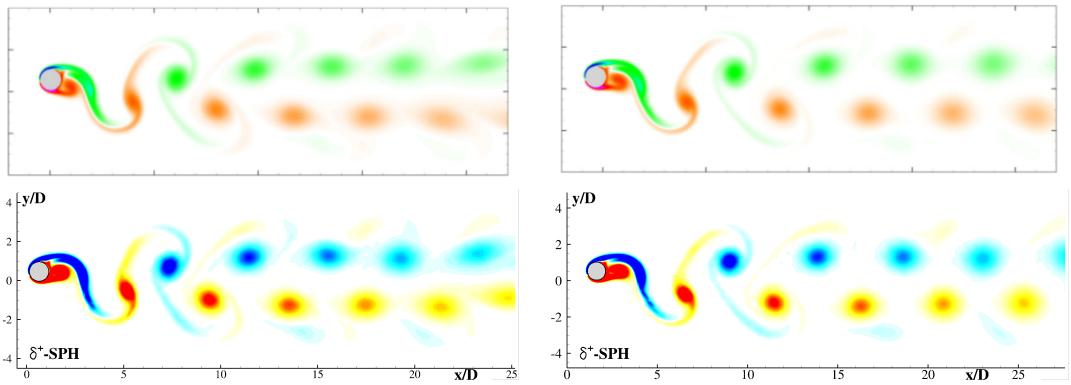

Figure 10: Snapshots of the vorticity fields at the maximum transverse displacement of the cylinder at two mass ratios: $m^* = 4/\pi$ (left) and $m^* = 0.5$ (right). The results through an immersed boundary method by Yang and Stern (2012)(top panels) are compared with the results of δ^+-SPH (bottom panels). Dimensionless vorticity $\omega\, D/U$ scales from -2.5 (blue) to 2.5 (red)

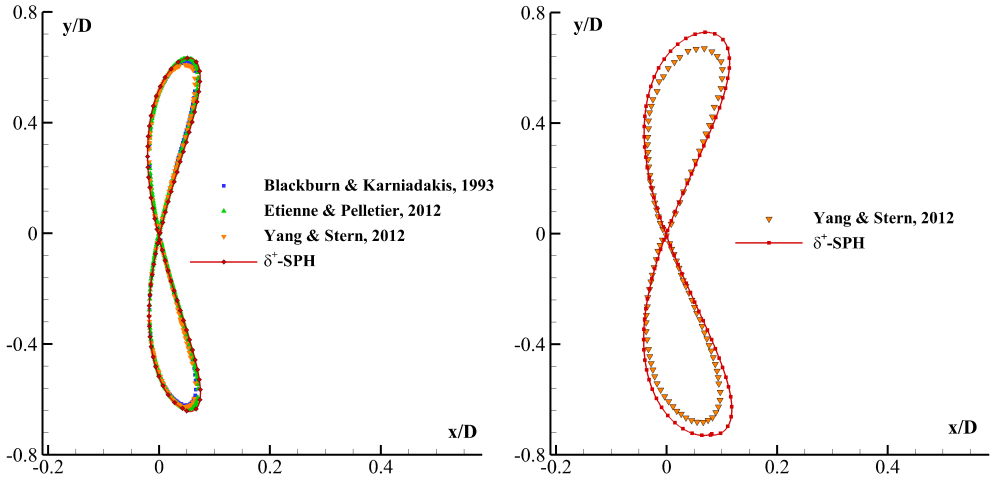

Figure 11: Trajectories of the cylinder motions in the two cases with different mass ratios: $m^* = 4/\pi$ (left) and $m^* = 0.5$ (right), the δ^+SPH results are compared against different reference solutions from Blackburn and Karniadakis (1993), Étienne and Pelletier (2012) and Yang and Stern (2012).

of the particle number of 90% compared to using a uniform particle resolution as $\Delta x = D/50$ in the whole fluid domain.

In this case the vortex shedding produces a periodical variation of the asymmetrical pressure distribution on the body surface and the resulting torque causes the rotational motion.

As stated in Robertson et al. (2003), the body's rotational motion in a VIV system is hard to treat with some mesh-based solvers, especially for cases with large rotation angles. Usually special techniques, like sliding mesh, re-meshing or immersed boundary techniques, are required to avoid numerical complexities due to the serious mesh distortions. Conversely, in a meshless method the amplitude of the rotation angle can be of arbitrary magnitudes and no extra numerical treatment is necessary.

Following Robertson et al. (2003), the governing equation with numerical damping for the body's rotational motion is written as follows:

$$\ddot{\theta} + 2\zeta_\theta \left(\frac{2\pi}{U_\theta^*}\right)\dot{\theta} + \left(\frac{2\pi}{U_\theta^*}\right)^2 \theta = \frac{C_T}{2I^*}, \tag{19}$$

where θ is the rotation angle (positive in the anti-clockwise direction) around the pivotal point which locates on the mass center. $\zeta_\theta = c_\theta/(2\sqrt{k_\theta I_S})$ in which c_θ is the torsional damping coefficient, k_θ the torsional spring

coefficient and I_S the moment of inertia. U_θ^* is the reduced velocity which is calculated by $U/(f_\theta D)$ where f_θ is the natural frequency and it is expressed as $f_\theta = 1/(2\pi)\sqrt{k_\theta/I_S}$. C_T is the coefficient of rotational torque which is expressed as $C_T = T/{}^1\!/_2\rho D^2 U^2$. I^* is the dimensionless moment of inertia which is equal to $I_S/\rho D^4$.

Two benchmarks, involving the rotations with moderate and large amplitudes, are tested in the following part. We use the same parameters as adopted by Yang and Stern (2012) with the Immersed Boundary Method (IBM) and Robertson et al. (2003) with the Spectral Element Method (SEM). The same parameters $I^* = 400$ and $U_\theta^* = 40$ are adopted for the two cases. The difference lies in the damping ratio for which $\zeta = 0.25$ is imposed in the first case restricting the rotational motion, while $\zeta = 0$ is assigned in the second case allowing for large rotations.

Time evolutions of the rotation angle under $\zeta = 0.25$ are shown in Figure 12 in which, during the steady stage when $tU/D > 400$, the oscillating amplitude of the δ^+SPH result shows a good agreement with the result obtained by Yang and Stern (2012) using IBM and the one obtained by Robertson et al. (2003) with SEM. The discrepancy observed at the initial stage when the rotational motion develops may due to the different time-ramp adopted for the free-stream velocity. During the steady stage, we can find a good agreement for the oscillating period in the results of δ^+SPH and SEM (Robertson et al., 2003), while a slight phase shift is observed in the IBM result by Yang and Stern (2012).

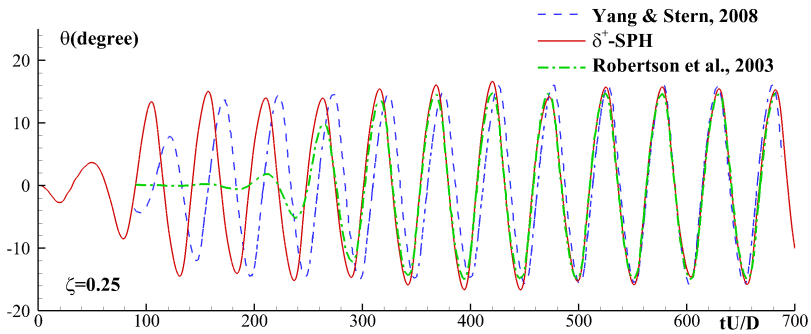

Figure 12: Time evolutions of the rotation angle for the rotational galloping with parameters of $Re = 200$, $L/D = 4$, $I^* = 400$, $U^* = 40$ and $\zeta = 0.25$; the δ^+SPH result is compared against the IBM result from Yang and Stern (2012) and the SEM result provided by Robertson et al. (2003).

In order to demonstrate the mechanism of the vortex induced rotation, the pressure and vorticity distributions around the rectangular body at three time instants are depicted in Figure 13. In the front shoulders of the rectangular body, vortices are developed alternately and shed under the rotational effect. On one of the two sides the boundary layer separates and generates an intense vortical structures which induces a low pressure region close to the body with a suction effect. On the other side the boundary layer remains attached with higher pressure levels. Those pressure differences cause the torque with respect to the pivotal point.

When the damping coefficient is reduced to $\zeta = 0$, the rotation angle excited by the vortex shedding is much larger. The SEM by Robertson et al.

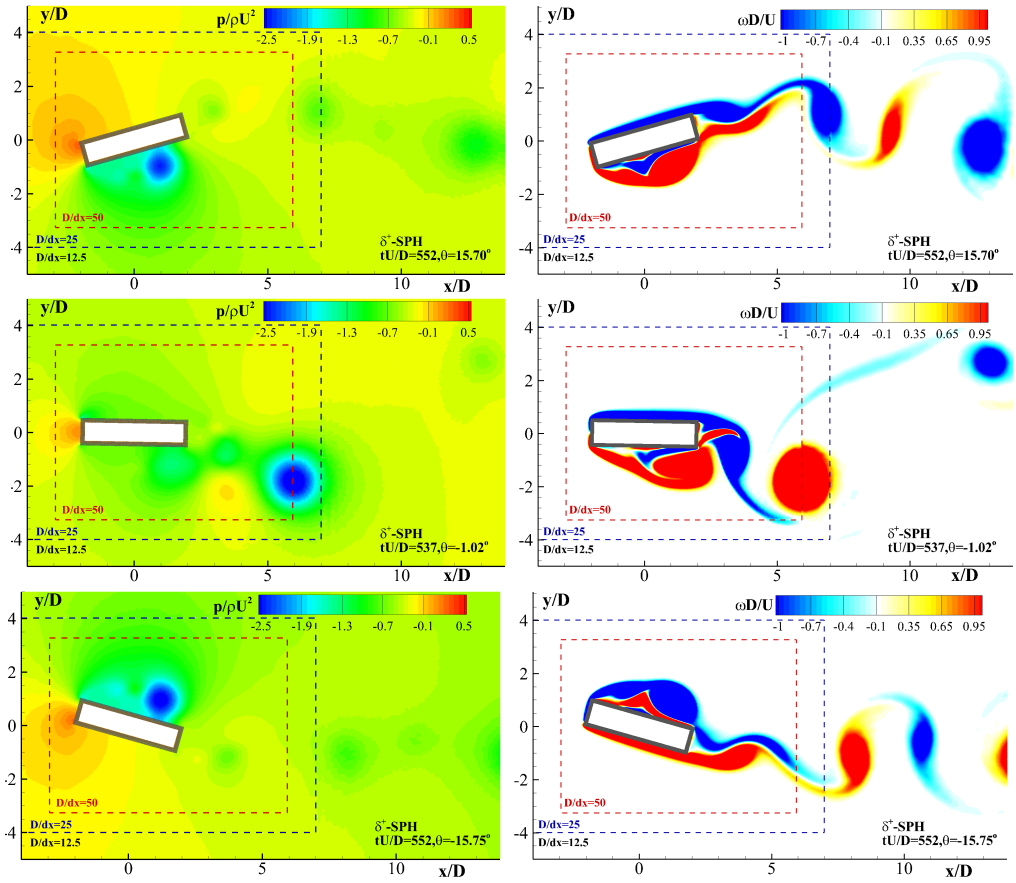

Figure 13: Snapshots of the pressure (left) and vorticity (right) fields around the rotating rectangular body at three time instants with the parameters of $Re = 200$, $L/D = 4$, $I^* = 400$, $U^* = 40$ and $\zeta = 0.25$.

(2003) failed to simulate this case due to the mesh distortion induced by the body's large rotation. The time evolution of the rotation angle predicted by δ^+SPH is plotted in Figure 14 together with the IBM result by Yang and Stern (2012). One can observe a good agreement between the results of δ^+-SPH and IBM of Yang and Stern (2012). A slight phase shift in the steady stage is observed, but the magnitude of the shift is much smaller comparing with the one observed in the last case of $\zeta = 0.25$.

After reducing the damping coefficient, the phenomenon of vortex shedding behind the rectangular body is much more complex than in the previous case. The vortex distributions at two maximum rotation angles ($tU/D = 493.5$, $\theta = -122.8°$ and $tU/D = 614.5$, $\theta = 125.3°$) and at one moderate angle ($tU/D = 505.5$, $\theta = 25.32°$) are depicted in Figure 15 where the mechanism of the vortex induced rotation can be analyzed through the fields of pressure and vorticity. It is shown that at the maximum angles, at the rear-edge of the cylinder, several vortices are shed simultaneously and a group of negative pressure regions are generated, while on the front-edge the flow separates generating a long shear layer causing pressure levels higher than around the rear part of the cylinder. As a consequence at these time instants a large torque is created and reverses the rotational direction. At the intermediate time $tU/D = 505.5$, a vortex group consisting of several structures is shed into the flow (see right hand side of Figure 15). Close to the body, new vortices are generated due to the flow separation around the

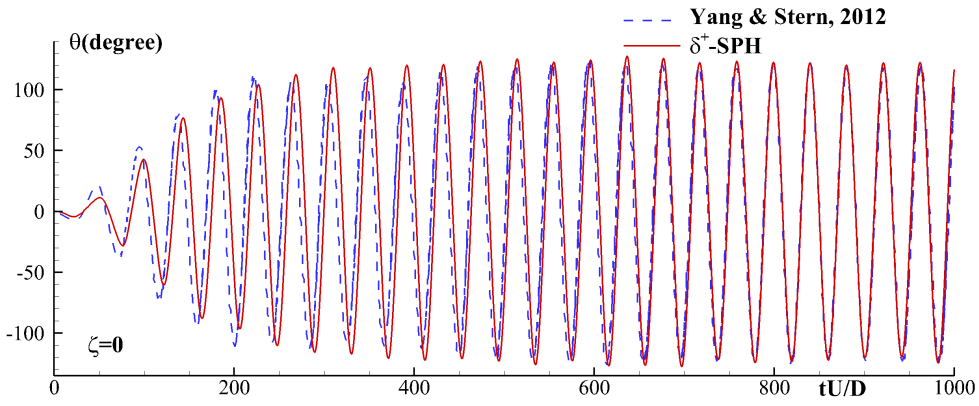

Figure 14: Time evolution of the rotation angle for the rotational galloping with parameters of $Re = 200$, $L/D = 4$, $I^* = 400$, $U^* = 40$ and $\zeta = 0$; the δ^+SPH and the IBM results from Yang and Stern (2012) are compared.

front and rear edges of the cylinder and the pressure variation due to these vortices accelerates the body's rotational motion.

Despite the large amplitude of the rotational motion and the complexity of vortical flow evolutions, the δ^+SPH model has also shown a satisfied stability and a sufficient accuracy in simulating this benchmark test-case.

3.6. Vortex induced motions of two galloping bodies

As a final test-case the vortex induced motions of two tandem positioned rectangular bodies, with the same width but different length ratios, are modelled. Multi-body interactions are observed due to the vortex shedding from the upstream body affecting the motion of the downstream one.

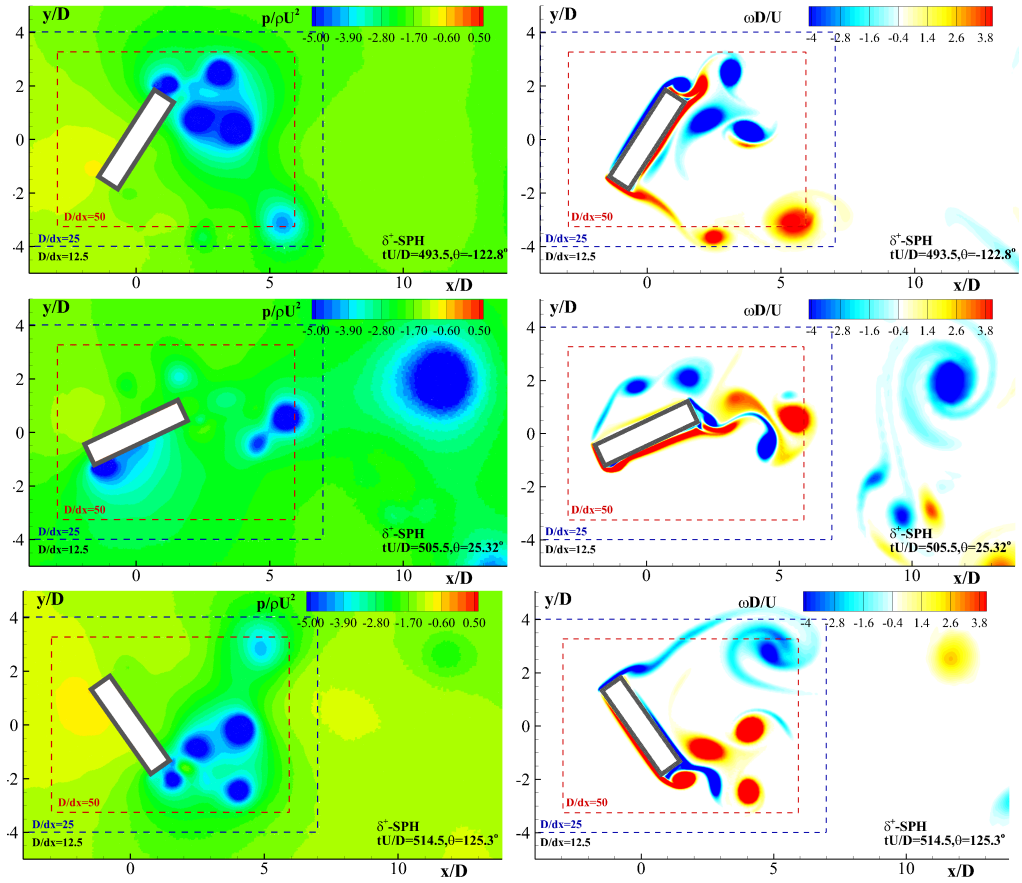

Figure 15: Snapshots of the pressure (left) and vorticity (right) fields around the rotating rectangular body at three time instants with the parameters of $Re = 200$, $L/D = 4$, $I^* = 400$, $U^* = 40$ and $\zeta = 0$.

In the framework of the δ^+SPH model, multi-body VIV problems can also be straightforwardly simulated with the coupling algorithm resented in Section 2.3. This benchmark has been presented by Yang and Stern (2012). It consists of a square body with the length ratio as $L = D$ in the upstream part while the second one in the downstream is a rectangular body with the length ratio as $L/D = 4$.

Similar to Yang and Stern (2012), the motions of the bodies are solved according to the following equations:

$$\begin{cases} \ddot{Y}_1 + 2\zeta_{Y_1}\left(\dfrac{2\pi}{U^*_{Y_1}}\right)\dot{Y}_1 + \left(\dfrac{2\pi}{U^*_{Y_1}}\right)^2 Y_1 = \dfrac{2C_{L_1}}{\pi m^*_1}, \\ \ddot{\theta}_2 + 2\zeta_{\theta_2}\left(\dfrac{2\pi}{U^*_{\theta_2}}\right)\dot{\theta}_2 + \left(\dfrac{2\pi}{U^*_{\theta_2}}\right)^2 \theta_2 = \dfrac{C_{T_2}}{2I^*_2}, \end{cases} \tag{20}$$

where the first equation describes the transverse oscillation of the square body with subscript 1 and the second equation describes the rotational motion of the rectangular body with subscript 2.

The Reynolds number in this problem is still set as Re=250 calculated using again D as reference length. In the governing equations of the body motion, parameters for the square body are $U^*_{Y_1} = 40$, $m^*_1 = 20$ and $\zeta_{Y_1} = 0.0037$ and parameters for the rectangular body are $U^*_{\theta_2} = 40$, $I^*_2 = 400$ and $\zeta_{\theta_2} = 0.25$ which are identical to the parameters of the first case discussed in Section 3.5. In this way, a comparison can be conducted to demonstrate the effect of the upstream body on the VIV motion of the downstream body.

Time evolutions of the responses of the two tandem arranged bodies are plotted in Figure 16, where the δ^+SPH results are compared to the ones obtained in Yang and Stern (2012). Top plot of the figure shows the time history of the vertical motion of the square body, while the bottom plot of the same figure depicts the time history of the galloping rotation angle of the second body. After a short transitional stage, when $tU/D \geq 200$, the motions of the two bodies enter in a periodic regime. Due to the complexity of the coupling interaction between the motions of the tandem arranged bodies, the galloping amplitude for each body in the time domain is not constant, see also Yang and Stern (2012), but good agreements between the two numerical results are obtained in the periodic regime ($tU/D \geq 200$) in terms of the average galloping amplitudes and their frequencies.

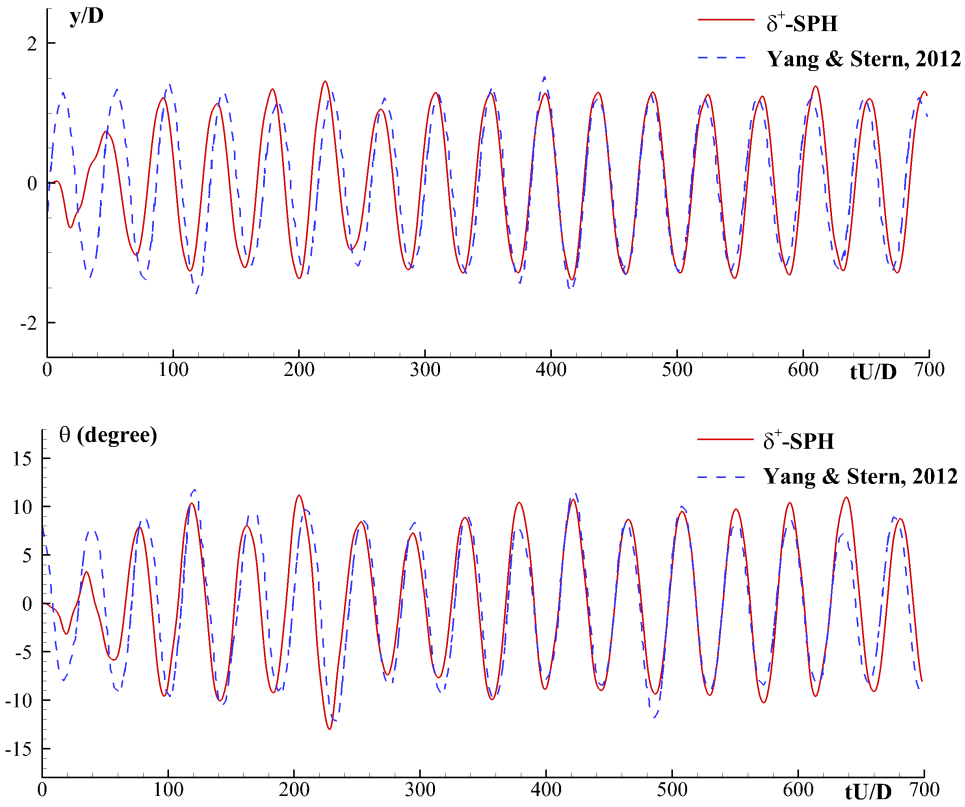

Figure 16: Time evolutions of the responses of the two tandem arranged bodies: the vertical oscillation of the square body on the top and the rotational motion of the rectangular body on the bottom; the δ^+SPH and the IBM results from Yang and Stern (2012) are compared.

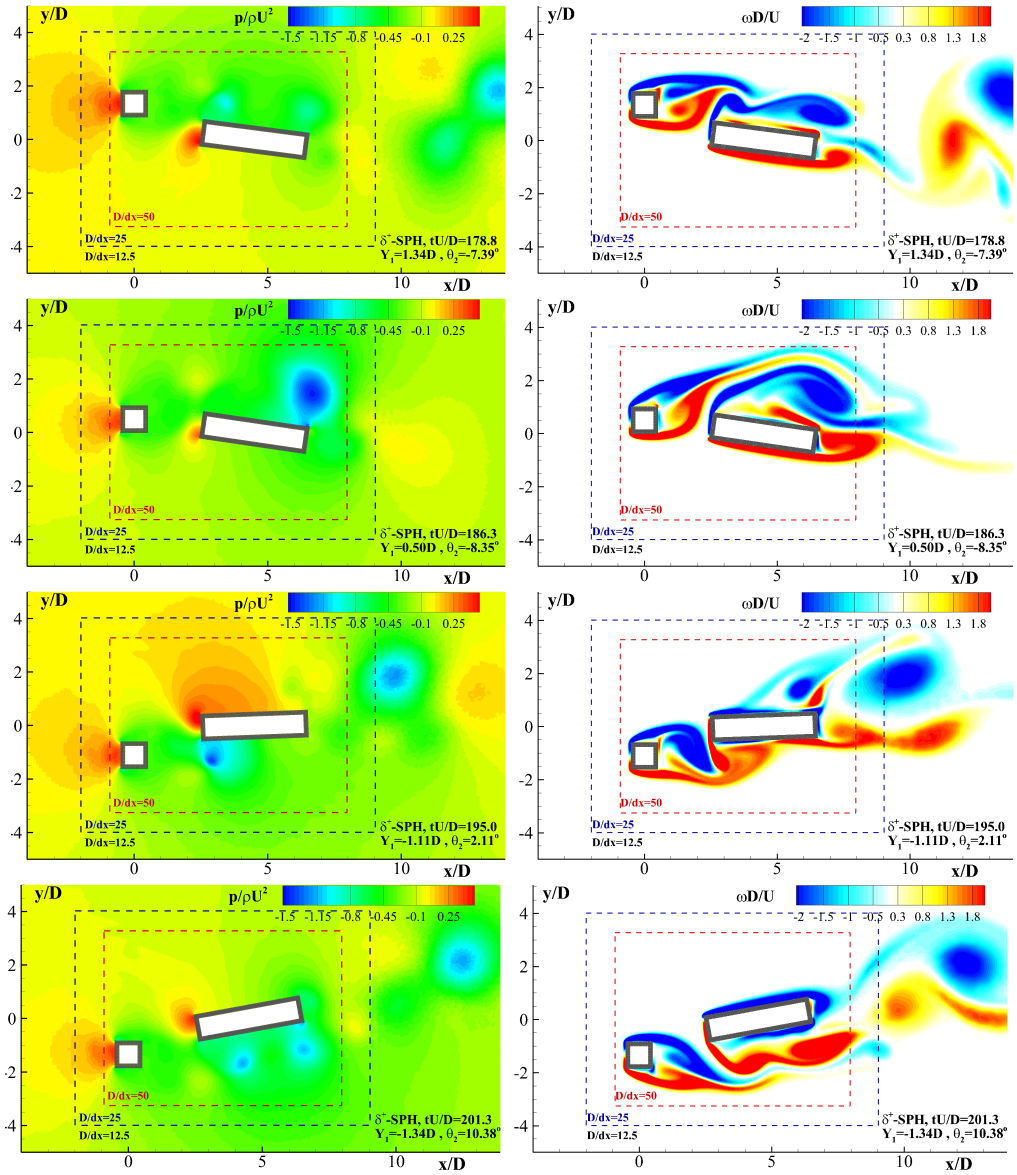

Figure 17: Snapshots of the pressure (left) and vorticity (right) fields around the galloping square and rectangular bodies at four time instants. The square body translates from the maximum vertical position (top) to the minimum one (bottom).

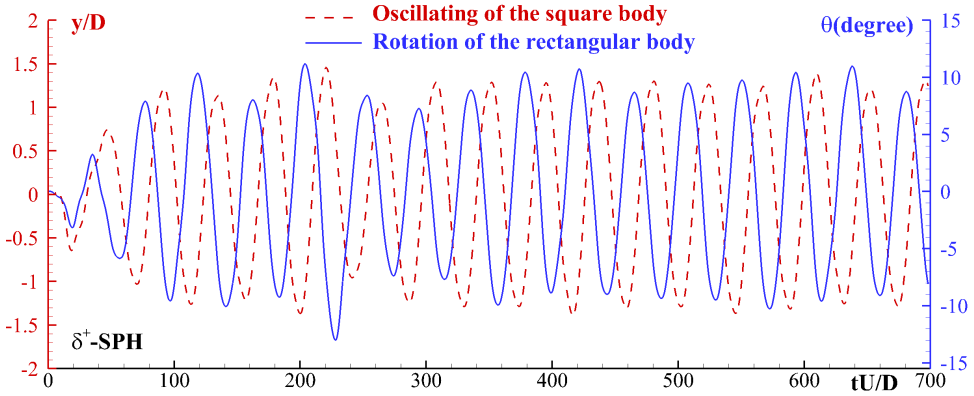

Figure 18: Time evolutions of the responses of the two tandem arranged bodies.

The pressure and vorticity distributions around the two bodies are depicted in Figure 17 at four time instants when the square body gradually translates from the maximum vertical position to the minimum one. It is interesting to find that the front edges of the rectangular body always follows the motion of the squared one. This can also be seen from Figure 18 where the responses of the two-body galloping are plotted together. The galloping frequencies of the two bodies are similar, but the rotational motion of the rectangular body is delayed with a certain phase angle.

The mechanism of the multi-body VIV problem can be analyzed through the pressure and vorticity plots. From the pressure field in Figure 17, it is possible to see that behind the square body, there is a region with lower pressure due to the viscous flow separation on the two cylinder front edges. This lower pressure region, vertical moving, contributes to the torque on the rectangular body which rotates towards the direction of the square body. Observing the vorticity field, it shows the lower pressure region behind the square body is due to the two counterrotating recirculation zones. Conversely, focusing on the vorticity around the rectangular body, those contour plots depict that the flow separations appear alternatively on the upper and on the bottom side. In particular the side where the flow separation occurs is the one much closer to the square body. Indeed, the flow separation is strengthened due to the suction effect from the vortex wake of the square body.

In addition to the pressure and vorticity plots, Lagrangian Coherent Structures (LCSs) detected by the backward-time FTLE are also detected

in this case to help revealing the VIV mechanism and understanding the flow features. As stated in Sun et al. (2016), LCSs can display the main flow features. Indeed, the LCSs can be found through algorithms based on the identification of the skeletons of the most repelling/attracting material surfaces in a flow. These skeletons act as inner boundaries that organize the main flow structures. LCSs can clearly show up the flow features like: vortex motion, flow separation, material transportation, exchanging and mixing, etc.

Figure 19 depicts the LCSs around the two coupled galloping bodies at eight time instants when the square body is translated from the maximum vertical position to the minimum one. The flow separation on the square occurs on the two front vertices while on the rectangular body, the position of flow separation switches on different sides during the body's rotation. At $tU/D = 178.8$ when the square body locates at the maximum transverse position, a flow gap, which is constructed by the LCSs shed from the two bodies, can be observed. The flow material past between the two bodies is transported through this flow gap. Since the fluid cannot penetrate the LCSs, the fluid is gradually entrained into the vortices behind the rectangular body.

As the square body moving downward during $tU/D \in [178.8, 192.5]$, the flow gap is firstly expanded and then closed. It is interesting to see that during $tU/D \in [192.5, 195]$, the closing of the flow gap coincides with the inversion of the rotation of the rectangular body from clockwise to anticlockwise. Form the subplot at $tU/D = 195$ in Figure 17, a large positive pressure can be observed at the instant of flow gap closing. After $tU/D = 195$ in Figure 19, as the square body further moves downward, a new flow gap is formed and a new accumulation of the vortex structures behind the rectangular body starts. During the duration when the square body moves from the lowest position to the highest, periodically a similar vortex accumulating and shedding process restarts.

From the above analysis, the motions of the two bodies are tightly coupled between each other, which explains why the frequencies of the two body motions are comparative but their phase angles have a certain shift between each other, see also in Figure 18. Further, due to the constrain of the vortex structure shed from the square body, as plotted in Figure 20, the magnitude of the rotation angle of the rectangular body is reduced when comparing against the result from the rotational galloping of an isolate rectangular body (see Section 3.5).

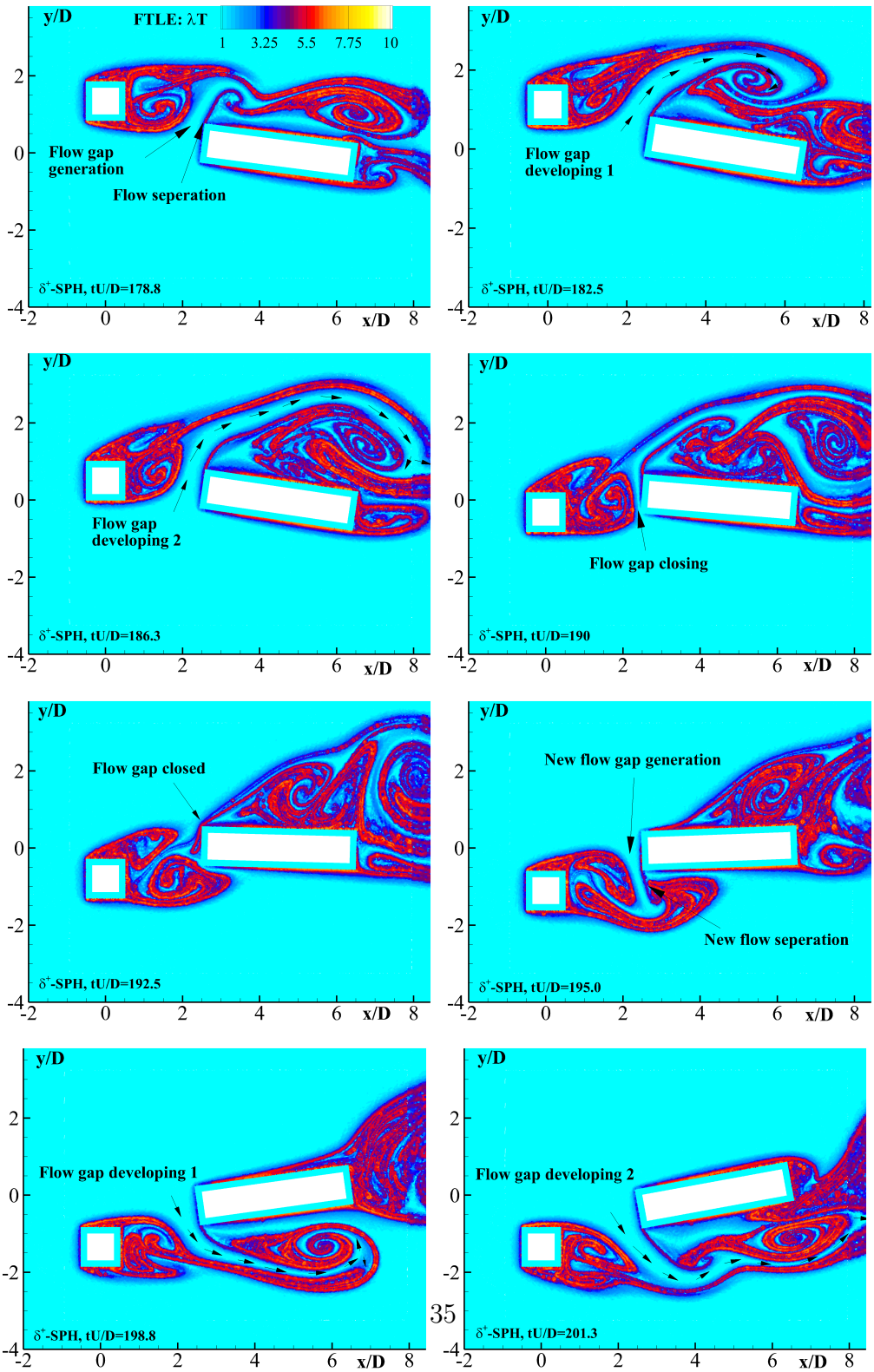

Figure 19: Distributions of the Lagrangian Coherent Structures around the two coupled galloping bodies at eight time instants when the upstream square body is translated from the maximum vertical position to the minimum one.

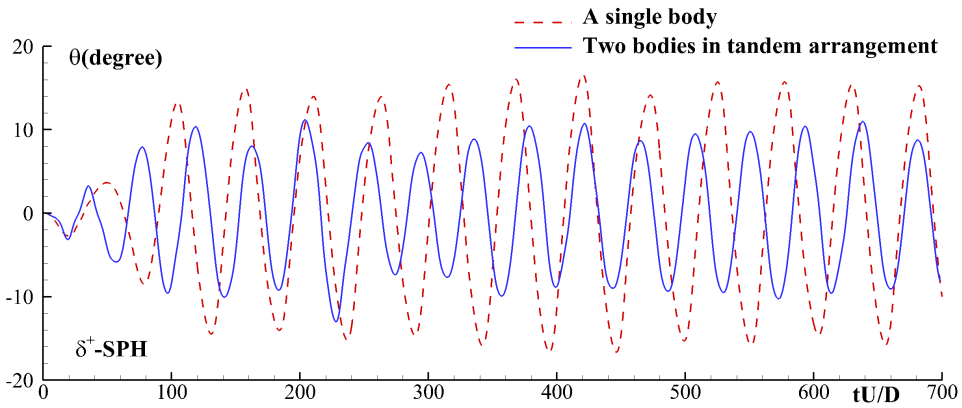

Figure 20: Time evolutions of the rotation angles in the rotational galloping: the result of an isolate rectangular body is compared with the one of two tandem arranged bodies.

4. Conclusions and future works

The recently developed δ^+SPH model is further extended in this paper to the modelling of VIV problems which, to the best of our knowledge, were rarely discussed in the SPH literature. Tensile Instability is completely removed in all the numerical results thanks to the TIC technique adopted in the region characterized by negative pressure.

Thanks to the mesh-free characteristic of the SPH method, the structure is allowed to perform translational and rotational motions in arbitrary amplitudes, avoiding any numerical issue caused by the distortion of the mesh topology. The adopted fluid-rigid body algorithm has been tested with cases characterized by very small mass ratios which were shown to be a critical condition in many other numerical solvers in the literature. Although the present coupled algorithm is established in an explicit manner, it has been shown to be capable of accurately solving many challenging VIV problems which could only be solved with a strong coupling technique. In addition, the coupling algorithm also allows for the simulation involving multi-body interactions.

In this work, the technique of adaptive particle refinement contributes to a considerable reduction of the entire computational cost and a significant increase of the numerical accuracy close to the body surface for resolving the viscous boundary layer. The particle shifting technique contributes to a regularized particle distribution which helps to remove the numerical

noise in the pressure/velocity field. Close to the body surface, the accurate evaluations of the pressure variation and the shear force in the boundary layer ensure an accurate prediction of the body motions. Inflow and outflow boundaries, which are quite challenging to be implemented in Lagrangian particles methods, have been shown to perform well within the viscous flow accompanying strong vortices.

All the SPH results have demonstrated an excellent agreement with the reference solutions. The numerical results show that the δ^+SPH model possesses most of the advantages of existing CFD solvers. In addition, thanks to the explicit tracking of all the particle trajectories, LCSs can be straightforwardly detected in the δ^+SPH model and it helps to understand the flow features from a Lagrangian point of view.

Since SPH is very suitable for the modelling of free surface flows, in future studies, the present SPH model can be straightforwardly applied to VIV problems under free-surface effects, such as the surface piercing structures (*e.g.* legs of offshore platforms, floating wind turbine, etc) which oscillates in ocean currents or waves under periodical hydrodynamic forces.

When the present δ^+SPH model is applied to three dimensional VIV problems of higher Reynolds numbers, the using of an advanced adaptive particle refinement technique to further improve the particle resolution in the thinner boundary layer is needed. The simulations in this paper are all run on a personal computer, but for three dimensional cases, parallel computations on high-performance clusters are needed. Further, appropriate turbulence models can also be included in this δ^+SPH model to properly consider turbulence effects. Lastly, the coupling of the present SPH model with mesh-based numerical method such as FVM is hopeful to reduce the computational cost in three dimensional applications (see *e.g.* Marrone et al. (2016); Chiron et al. (2018a).

5. Acknowledgements

The author PengNan Sun is funded by a post-doctoral research grant from Ecole Centrale Nantes. A-Man Zhang is funded by the National Project of Numerical Wind Tunnel of China (Grant No. 2018-ZT2B05) and the National Natural Science Foundation of China (Grant No. 11872158).

The research activity has also been developed within the Project Area "Applied Mathematics" of the Department of Engineering, ICT and

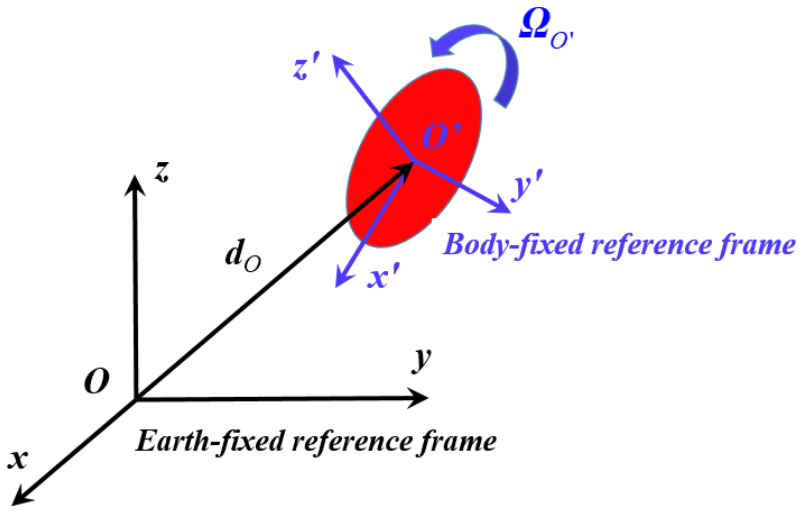

Figure A.21: Illustration of the earth-fixed (inertial) and body-fixed (non-inertial) reference frames for the solving of the fluid-solid interactions.

Technology for Energy and Transport (DIITET) of the Italian National Research Council (CNR).

Appendix A. 3D Rigid body motion dynamics

In the present section the rigid body dynamics presented in Section 2.3 is generalized to a three-dimensional framework. The translational motion of the body is solved within the earth-fixed frame and the rotational one is updated in the body-fixed reference frame (see the illustration in Figure A.21). Following the notation of Section 2.3, the origin of coordinates of the body-fixed frame locating at the body's mass-center is denoted by subscript O in the earth-fixed frame while subscript O' refers to the body fixed frame.

Following the sketch in Figure A.21, the variables for updating the body position and orientation can be summarized as

$$\boldsymbol{y}_b = \Big(..., \dot{\boldsymbol{U}}_{\boldsymbol{O}}, \boldsymbol{U}_{\boldsymbol{O}}, \boldsymbol{d}_{\boldsymbol{O}}, \dot{\boldsymbol{\Omega}}_{\boldsymbol{O'}}, \boldsymbol{\Omega}_{\boldsymbol{O'}}, \boldsymbol{\theta}_{\boldsymbol{O}}, ...\Big). \tag{A.1}$$

The rotation of the body is expressed through Euler angles:

$$\boldsymbol{\theta}_{\boldsymbol{O}} = [\alpha, \beta, \gamma]^T, \tag{A.2}$$

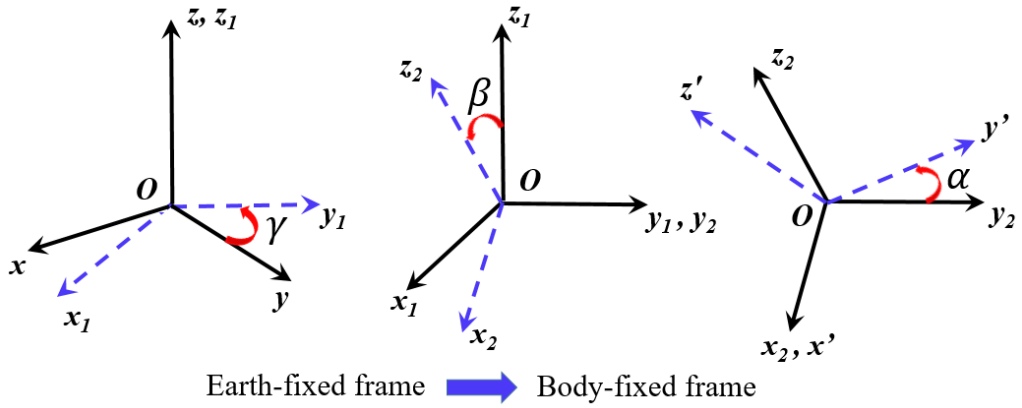

Figure A.22: Rotation from the earth-fixed frame to the body-fixed frame by Euler angles.

where T denotes the transpose operation. Following the sketch of Figure A.22, in connections to the Euler angles the corresponding matrices of rotation are defined as:

$$\mathbb{R}_\alpha = \begin{bmatrix} 1 & 0 & 0 \\ 0 & \cos\alpha & \sin\alpha \\ 0 & -\sin\alpha & \cos\alpha \end{bmatrix}, \mathbb{R}_\beta = \begin{bmatrix} \cos\beta & 0 & -\sin\beta \\ 0 & 1 & 0 \\ \sin\beta & 0 & \cos\beta \end{bmatrix}, \mathbb{R}_\gamma = \begin{bmatrix} \cos\gamma & \sin\gamma & 0 \\ -\sin\gamma & \cos\gamma & 0 \\ 0 & 0 & 1 \end{bmatrix} \quad \text{(A.3)}$$

With the defined matrices the coordinate in the earth-fixed frame can be transformed to the body-fixed frame as

$$\boldsymbol{r}' = \mathbb{R}_\alpha \mathbb{R}_\beta \mathbb{R}_\gamma \boldsymbol{r}. \quad \text{(A.4)}$$

Inverting the above relation, the coordinate of j-th particle/node attached to the solid body can be written in the earth-fixed frame as:

$$\boldsymbol{r}_j = \boldsymbol{d}_{\boldsymbol{O}} + \mathbb{R} \cdot \boldsymbol{r'}_j, \qquad \mathbb{R} := \mathbb{R}_\gamma^T \mathbb{R}_\beta^T \mathbb{R}_\alpha^T, \quad \text{(A.5)}$$

where $\boldsymbol{r}'_j$ is the vector representing the coordinate of particle j in the body-fixed frame (non-inertial reference frame, see Figure A.21), while $\mathbb{R}$ is the global rotation matrix.

The angular velocity of the rigid body in the body-fixed reference frame and the time derivative of the Euler angle have the following relation:

$$\boldsymbol{\Omega}_{\boldsymbol{O'}} = \begin{bmatrix} \dot{\alpha} \\ 0 \\ 0 \end{bmatrix} + \mathbb{R}_\alpha \begin{bmatrix} 0 \\ \dot{\beta} \\ 0 \end{bmatrix} + \mathbb{R}_\alpha \mathbb{R}_\beta \begin{bmatrix} 0 \\ 0 \\ \dot{\gamma} \end{bmatrix}. \quad \text{(A.6)}$$

Inverting the above equation we get:

$$\dot{\boldsymbol{\theta}}_{\boldsymbol{O}} = \mathbb{J}\,\boldsymbol{\Omega}_{\boldsymbol{O'}}, \qquad \mathbb{J} := \begin{bmatrix} 1 & \sin\alpha\tan\beta & \cos\alpha\tan\beta \\ 0 & \cos\alpha & -\sin\alpha \\ 0 & \sin\alpha/\cos\beta & \cos\alpha/\cos\beta \end{bmatrix}. \tag{A.7}$$

Finally, the governing equations for the translational and rotational accelerations of the rigid body can be written in the three-dimensional framework as:

$$\begin{cases} M\dot{\boldsymbol{U}}_{\boldsymbol{O}} = \boldsymbol{F}_{\boldsymbol{O}} + M\boldsymbol{g}, \\ \boldsymbol{I}_{\boldsymbol{O'}}\dot{\boldsymbol{\Omega}}_{\boldsymbol{O'}} + \boldsymbol{\Omega}_{\boldsymbol{O'}} \times \boldsymbol{I}_{\boldsymbol{O'}}\boldsymbol{\Omega}_{\boldsymbol{O'}} = \boldsymbol{T}_{\boldsymbol{O'}}, \end{cases} \tag{A.8}$$

where M is the body mass and $\boldsymbol{I}_{\boldsymbol{O'}}$ the moment of inertia with respect to the mass center $\boldsymbol{O'}$ in the body-fixed frame. The torque $\boldsymbol{T}_{\boldsymbol{O'}}$ in the body fixed frame can be obtained as

$$\boldsymbol{T}_{\boldsymbol{O'}} = \mathbb{R}^T\boldsymbol{T}_{\boldsymbol{O}}. \tag{A.9}$$

The positions, velocities and accelerations of the solid surface nodes can be updated as

$$\begin{cases} \boldsymbol{u}_j = \boldsymbol{U}_{\boldsymbol{O}} + \boldsymbol{\Omega}_{\boldsymbol{O}} \times \boldsymbol{r}_j, \\ \boldsymbol{a}_j = \dot{\boldsymbol{U}}_{\boldsymbol{O}} + \dot{\boldsymbol{\Omega}}_{\boldsymbol{O}} \times \boldsymbol{r}_j + \boldsymbol{\Omega}_{\boldsymbol{O}} \times (\boldsymbol{\Omega}_{\boldsymbol{O}} \times \boldsymbol{r}_j), \end{cases} \tag{A.10}$$

where $\boldsymbol{\Omega}_{\boldsymbol{O}}$ can be obtained using the rotation matrix $\mathbb{R}$ from $\boldsymbol{\Omega}_{\boldsymbol{O'}}$.

References

M. Antuono, A. Colagrossi, S. Marrone, and D. Molteni. Free-surface flows solved by means of SPH schemes with numerical diffusive terms. *Computer Physics Communications*, 181(3):532–549, 2010.

M. Antuono, A. Colagrossi, and S. Marrone. Numerical diffusive terms in weakly-compressible sph schemes. *Computer Physics Communications*, 183 (12):2570–2580, 2012.

M. Antuono, B. Bouscasse, A. Colagrossi, and S. Marrone. A measure of spatial disorder in particle methods. *Computer Physics Communications*, 185(10):2609–2621, 2014.

M. Antuono, S. Marrone, A. Colagrossi, and B. Bouscasse. Energy balance in the δ-SPH scheme. *Computer Methods in Applied Mechanics and Engineering*, 289:209–226, 2015.

D.A. Barcarolo, D. Le Touzé, G. Oger, and F. de Vuyst. Adaptive particle refinement and derefinement applied to the smoothed particle hydrodynamics method. *Journal of Computational Physics*, 273:640–657, 2014.

P.W. Bearman. Circular cylinder wakes and vortex-induced vibrations. *Journal of Fluids and Structures*, 27(5):648–658, 2011.

H.M. Blackburn and G.E. Karniadakis. Two-and three-dimensional simulations of vortex-induced vibration or a circular cylinder. In *The Third International Offshore and Polar Engineering Conference*. International Society of Offshore and Polar Engineers, 1993.

B. Bouscasse, A. Colagrossi, S. Marrone, and M. Antuono. Nonlinear water wave interaction with floating bodies in SPH. *Journal of Fluids and Structures*, 42:112–129, 2013.

M. Braza, P. Chassaing, and H. Minh. Numerical study and physical analysis of the pressure and velocity fields in the near wake of a circular cylinder. *Journal of Fluid Mechanics*, 165:79–130, 1986.

J.L. Cercos-Pita, M. Antuono, A. Colagrossi, and A. Souto-Iglesias. SPH energy conservation for fluid–solid interactions. *Computer Methods in Applied Mechanics and Engineering*, 317:771–791, 2017.

L. Chiron, S. Marrone, A. Di Mascio, and D. Le Touzé. Coupled SPH–FV method with net vorticity and mass transfer. *Journal of Computational Physics*, 364:111136, 2018a.

L. Chiron, G. Oger, M. De Leffe, and D. Le Touzé. Analysis and improvements of adaptive particle refinement (APR) through cpu time, accuracy and robustness considerations. *Journal of Computational Physics*, 354:552–575, 2018b.

A. Colagrossi, M. Antuono, and D. Le Touzé. Theoretical considerations on the free-surface role in the smoothed-particle-hydrodynamics model. *Physical Review E*, 79(5):056701, 2009.

879 A. Colagrossi, M. Antuono, A. Souto-Iglesias, and D. Le Touzé. Theoretical
880 analysis and numerical verification of the consistency of viscous smoothed-
881 particle-hydrodynamics formulations in simulating free-surface flows.
882 *Physical Review E*, 84:026705, 2011.

883 A. Colagrossi, E. Rossi, S. Marrone, and D. Le Touzé. Particle Methods
884 for Viscous Flows: Analogies and Differences Between the SPH and
885 DVH Methods. *Communications in Computational Physics*, 20(3):660–
886 688, 2016.

887 J. Deng, X.M. Shao, and Z.S. Yu. Hydrodynamic studies on two traveling
888 wavy foils in tandem arrangement. *Physics of fluids*, 19(11):113104, 2007.

889 M. Ellero and N.A. Adams. SPH simulations of flow around a periodic array
890 of cylinders confined in a channel. *International Journal for Numerical*
891 *Methods in Engineering*, 86(8):1027–1040, 2011.

892 S. Étienne and D. Pelletier. The low reynolds number limit of vortex-induced
893 vibrations. *Journal of Fluids and Structures*, 31:18–29, 2012.

894 H. Falahaty, A. Khayyer, and H. Gotoh. Enhanced particle method with
895 stress point integration for simulation of incompressible fluid-nonlinear
896 elastic structure interaction. *Journal of Fluids and Structures*, 81:325–360,
897 2018.

898 I. Federico, S. Marrone, A. Colagrossi, F. Aristodemo, and M. Antuono.
899 Simulating 2D open-channel flows through an SPH model. *European*
900 *Journal of Mechanics-B/Fluids*, 34:35–46, 2012.

901 R.K. Jaiman, N.R. Pillalamarri, and M.Z. Guan. A stable second-order
902 partitioned iterative scheme for freely vibrating low-mass bluff bodies in a
903 uniform flow. *Computer Methods in Applied Mechanics and Engineering*,
904 301:187–215, 2016.

905 E. Kazemi, A. Nichols, S. Tait, and S.D. Shao. SPH modelling of depth-
906 limited turbulent open channel flows over rough boundaries. *International*
907 *journal for numerical methods in fluids*, 83(1):3–27, 2017.

908 A. Khayyer, H. Gotoh, and Y. Shimizu. Comparative study on accuracy
909 and conservation properties of two particle regularization schemes and

proposal of an optimized particle shifting scheme in ISPH context. *Journal of Computational Physics*, 332:236–256, 2017.

M. Lastiwka, M. Basa, and N. Quinlan. Permeable and non-reflecting boundary conditions in SPH. *International journal for numerical methods in fluids*, 61(7):709–724, 2009.

D.F. Liang, W. Jian, S.D. Shao, R.D. Chen, and K.J. Yang. Incompressible SPH simulation of solitary wave interaction with movable seawalls. *Journal of Fluids and Structures*, 69:72–88, 2017.

S.J. Lind, R. Xu, P.K. Stansby, and B.D. Rogers. Incompressible smoothed particle hydrodynamics for free-surface flows: A generalised diffusion-based algorithm for stability and validations for impulsive flows and propagating waves. *Journal of Computational Physics*, 231(4):1499–1523, 2012.

C. Liu, X. Zheng, and C.H. Sung. Preconditioned multigrid methods for unsteady incompressible flows. *Journal of Computational Physics*, 139(1): 35–57, 1998.

M.B. Liu and G.R. Liu. Smoothed particle hydrodynamics (SPH): an overview and recent developments. *Archives of computational methods in engineering*, 17(1):25–76, 2010.

M.B. Liu and Z.L. Zhang. Smoothed particle hydrodynamics (SPH) for modeling fluid-structure interactions. *Science China Physics, Mechanics & Astronomy*, 62(8):984701, 2019.

X. Liu, P.Z. Lin, and S.D. Shao. An ISPH simulation of coupled structure interaction with free surface flows. *Journal of Fluids and Structures*, 48: 46–61, 2014.

S. Marrone, A. Colagrossi, D. Le Touzé, and G. Graziani. Fast free-surface detection and level-set function definition in SPH solvers. *Journal of Computational Physics*, 229(10):3652–3663, 2010.

S. Marrone, M. Antuono, A. Colagrossi, G. Colicchio, D. Le Touzé, and G. Graziani. Delta-SPH model for simulating violent impact flows. *Computer Methods in Applied Mechanics and Engineering*, 200(13-16): 1526–1542, 2011a.

S. Marrone, A. Colagrossi, M. Antuono, C. Lugni, and M.P. Tulin. A 2D+t SPH model to study the breaking wave pattern generated by fast ships. *Journal of Fluids and Structures*, 27(8):1199–1215, 2011b.

S. Marrone, A. Di Mascio, and D. Le Touzé. Coupling of smoothed particle hydrodynamics with finite volume method for free-surface flows. *Journal of Computational Physics*, 310:161180, 2016.

J.R. Meneghini and P.W. Bearman. Numerical simulation of high amplitude oscillatory flow about a circular cylinder. *Journal of Fluids and Structures*, 9(4):435–455, 1995.

J.J. Monaghan. Smoothed particle hydrodynamics. *Reports on Progress in Physics*, 68:1703–1759, 2005.

J.J. Monaghan and R.A. Gingold. Shock Simulation by the particle method SPH. *Journal of Computational Physics*, 52(2):374–389, 1983.

Y.T. Ng, C.H. Min, and F. Gibou. An efficient fluid–solid coupling algorithm for single-phase flows. *Journal of Computational Physics*, 228(23):8807–8829, 2009.

I. Robertson, L. Li, S.J. Sherwin, and P.W. Bearman. A numerical study of rotational and transverse galloping rectangular bodies. *Journal of Fluids and Structures*, 17(5):681–699, 2003.

E. Rossi, A. Colagrossi, B. Bouscasse, and G. Graziani. The Diffused Vortex Hydrodynamics method. *Communications in Computational Physics*, 18 (2):351–379, 2015.

E. Rossi, A. Colagrossi, D. Durante, and G. Graziani. Simulating 2D viscous flow around geometries with vertices through the Diffused Vortex Hydrodynamics method. *Computer Methods in Applied Mechanics and Engineering*, 302:147–169, APR 15 2016.

M.S. Shadloo, A. Zainali, S.H. Sadek, and M. Yildiz. Improved incompressible smoothed particle hydrodynamics method for simulating flow around bluff bodies. *Computer methods in applied mechanics and engineering*, 200(9-12):1008–1020, 2011.

M.S. Shadloo, G. Oger, and D. Le Touzé. Smoothed particle hydrodynamics method for fluid flows, towards industrial applications: Motivations, current state, and challenges. *Computers & Fluids*, 136:11–34, 2016.

P.N. Sun, A. Colagrossi, S. Marrone, and A.M. Zhang. Detection of lagrangian coherent structures in the SPH framework. *Computer Methods in Applied Mechanics and Engineering*, 305:849–868, 2016.

P.N. Sun, A. Colagrossi, S. Marrone, and A.M. Zhang. The δplus-SPH model: Simple procedures for a further improvement of the SPH scheme. *Computer Methods in Applied Mechanics and Engineering*, 315:25–49, 2017.

P.N. Sun, A. Colagrossi, S. Marrone, M. Antuono, and A.M. Zhang. Multi-resolution Delta-plus-SPH with tensile instability control: towards high Reynolds number flows. *Computer Physics Communications*, 224:63–80, 2018a.

P.N. Sun, A. Colagrossi, and A.M. Zhang. Numerical simulation of the self-propulsive motion of a fishlike swimming foil using the δ^+-SPH model. *Theoretical and Applied Mechanics Letters*, 8(2):115–125, 2018b.

P.N. Sun, F.R. Ming, A.M. Zhang, and B. Wang. Viscous flow past a NACA0012 foil below a free surface through the Delta-Plus-SPH method. *International Journal of Computational Methods*, page 1846007, 2018c.

P.N. Sun, A. Colagrossi, S. Marrone, M. Antuono, and A.-M. Zhang. A consistent approach to particle shifting in the δ-Plus-SPH model. *Computer Methods in Applied Mechanics and Engineering*, 348:912–934, 2019.

A. Tafuni, J.M. Domínguez, R. Vacondio, and A.J.C. Crespo. A versatile algorithm for the treatment of open boundary conditions in smoothed particle hydrodynamics GPU models. *Computer Methods in Applied Mechanics and Engineering*, 342:604–624, 2018.

M. Tanaka, R. Cardoso, and H. Bahai. Multi-resolution MPS method. *Journal of Computational Physics*, 359:106–136, 2018.

R. Vacondio, B.D. Rogers, P.K. Stansby, P. Mignosa, and J. Feldman. Variable resolution for SPH: a dynamic particle coalescing and splitting scheme. *Computer Methods in Applied Mechanics and Engineering*, 2013.

E.H. Wang, Q. Xiao, and A. Incecik. Three-dimensional numerical simulation of two-degree-of-freedom VIV of a circular cylinder with varying natural frequency ratios at Re= 500. *Journal of Fluids and Structures*, 73:162–182, 2017.

H. Wendland. Piecewise polynomial, positive definite and compactly supported radial functions of minimal degree. *Adv. Comput. Math.*, 4 (4):389–396, 1995.

C.H.K. Williamson and R. Govardhan. Vortex-induced vibrations. *Annu. Rev. Fluid Mech.*, 36:413–455, 2004.

C.H.K. Williamson and R. Govardhan. A brief review of recent results in vortex-induced vibrations. *Journal of Wind Engineering and Industrial Aerodynamics*, 96(6):713–735, 2008.

X.D. Wu, F. Ge, and Y.S. Hong. A review of recent studies on vortex-induced vibrations of long slender cylinders. *Journal of Fluids and Structures*, 28: 292–308, 2012.

J. Yang, S. Preidikman, and E. Balaras. A strongly coupled, embedded-boundary method for fluid–structure interactions of elastically mounted rigid bodies. *Journal of Fluids and Structures*, 24(2):167–182, 2008.

J.M. Yang and F. Stern. A simple and efficient direct forcing immersed boundary framework for fluid–structure interactions. *Journal of Computational Physics*, 231(15):5029–5061, 2012.

A.M. Zhang, P.N. Sun, F.R. Ming, and A. Colagrossi. Smoothed particle hydrodynamics and its applications in fluid-structure interactions. *Journal of Hydrodynamics, Ser. B*, 29(2):187–216, 2017.

Z.L. Zhang and M.B. Liu. A decoupled finite particle method for modeling incompressible flows with free surfaces. *Applied Mathematical Modelling*, 60:606–633, 2018.

Z.L. Zhang, K. Walayat, C. Huang, J.Z. Chang, and M.B. Liu. A finite particle method with particle shifting technique for modeling particulate flows with thermal convection. *International Journal of Heat and Mass Transfer*, 128:1245–1262, 2019.